Nuclear Materials and Energy 39 (2024) 101683

Contents lists available at ScienceDirect

Nuclear Materials and Energy

journal homepage: www.elsevier.com/locate/nme

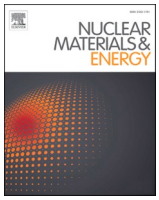

Additive manufacturing of novel complex tungsten components via electron beam melting: Basic properties and evaluation of the high heat flux behavior

Steffen Antusch [a,*], Alexander Klein [a], Siegfried Baumgärtner [a], Carsten Bonnekoh [a], Bernd Böswirth [b], Daniel Dorow-Gerspach [c], Stefan Dietrich [a], Marco Ehrhardt [a], Bradut-Eugen Ghidersa [a], Henri Greuner [b], Markus Guttmann [a], Thomas Hanemann [a], Judith Jung [a], Joachim Konrad [a], Michael Rieth [a]

[a] Karlsruhe Institute of Technology, Karlsruhe, Germany
[b] Max-Planck-Institut für Plasmaphysik, Garching, Germany
[c] Forschungszentrum Jülich GmbH, Institute of Energy and Climate Research, Partner of the Trilateral Euregio Cluster (TEC), Jülich, Germany

ARTICLE INFO

Keywords:
Additive manufacturing
Refractory metal
Tungsten
Electron beam melting
Plasma-facing unit
Mock-up
Copper cooling structure
Copper melt infiltration
Selective laser melting
Computational fluid dynamic calculations
Mechanical testing
High heat flux testing

ABSTRACT

The basic principle of electron beam melting (EBM) technology is the additive generation of structures by the selective melting of metal powder layer by layer with an electron beam under vacuum conditions. The cooling rate of the EBM process can be reduced drastically by increasing the temperature of the powder bed to avoid the formation of solidification cracks by brittle materials such as tungsten (W). This refractory metal is a promising candidate as plasma facing material for future fusion reactors. The selection of tungsten is owing to its physical properties such as the melting point of 3420 °C, the high strength and high thermal conductivity, the low thermal expansion and low erosion rate. Disadvantages are the low ductility, and fracture toughness at room temperature. Furthermore, the manufacturing by mechanical machining, such as milling and turning, is extremely cost and time consuming. An interesting alternative process route to conventional manufacturing technologies is EBM. It allows the near-net shape fabrication of prototype structures with geometrical freedom and has proven its capability for mass production by the manufacturing of hip prostheses made of titanium.

This manuscript describes the fabrication of tungsten parts via electron beam melting, with application to the manufacturing of divertor armour. The investigation comprises the microstructure examination, crystallographic texture, as well as mechanical characterization via tensile and Charpy impact testing. This is followed by the presentation of process routes to fabricate mock-ups with different designs and copper cooling structures.

Furthermore, the different mock-ups were exposed to high heat flux (HHF) applying transient thermal loads to assess thermal shock and thermal fatigue performance of EBM tungsten.

Post mortem analyses were performed quantifying the occurring damage with respect to reference tungsten grades by microscopical means.

The achieved results demonstrate the high potential to process tungsten via electron beam melting.

Introduction

Tungsten is a body-centered cubic (bcc) brittle refractory metal with the chemical symbol W and atomic number 74. Due to the high density (19.25 g/cm^3), high thermal conductivity (174 W/(m*K) at room temperature), high melting point (3420 °C), high strength and hardness, low thermal expansion and hydrogen interactions, tungsten has numerous applications [1–3]. X-ray and radiation protection for medical technology, electrodes for welding, components for high-temperature furnaces, and wear-resistant parts for rocket nozzles typical applications. Low activation (as compared to molybdenum) and low H-retention makes tungsten attractive for plasma-facing components for fusion reactors. The divertor concept of the world s largest fusion experiment presently under construction, the International Thermonuclear Experimental

* Corresponding author.
E-mail address: steffen.antusch@kit.edu (S. Antusch).

https://doi.org/10.1016/j.nme.2024.101683
Received 8 March 2024; Received in revised form 23 May 2024; Accepted 27 May 2024
Available online 28 May 2024

Reactor (ITER), is based on tungsten monoblocks as plasma-facing material. The tungsten monoblocks are connected to CuCrZr-pipes by different manufacturing technologies [4]. To qualify the involved processes and materials, small units of the real components were fabricated (so-called mock-ups) and their performance was determined by high heat flux (HHF) tests [5].

Industrially produced tungsten (W) grades are available in different types of semi-finished products, e.g. as rods, plates, and sheets. Conditioned by the powder metallurgical fabrication route (powder compaction, sintering, rolling or forging) the products show a relatively high density and are available in large quantities. However, the subsequent mechanical machining is very time-consuming and cost-intensive. An alternative method to conventional fabrication by material removal is additive manufacturing (AM). The potentials benefits of AM are rapid prototyping and the freedom in geometrical design to fabricate near-net shapes. In the past few years, several AM techniques have been developed and optimized. Common AM techniques for fabricating tungsten parts are laser powder-bed-fusion (LPBF), also known as selective laser melting (SLM), wire arc additive manufacturing (WAAM), and electron beam powder-bed-fusion (EBPBF), also known as electron beam melting (EBM). Regarding the before mentioned processes is given in [6–14]. To melt the metal powder the SLM process uses energy provided by a laser beam while the maximum laser power is < 1 kW. During the EBM process, the energy for melting the powder is generated by an electron beam (maximum electron beam power 3 kW). Independent of the power source, SLM and EBM have in common that the powder bed is melted selectively, layer-by-layer under a vacuum atmosphere. During the fabrication process, the cooling rate and the temperature gradient play an important role. Both are process-related and have a strong impact on the material properties and thus may influence the residual stresses and cracking behavior. Since the SLM process generally employs high cooling rates, brittle materials, such as tungsten, exhibit the formation of solidification cracks [15–18]. However, recent work in LPBF has shown, that crack formation can be minimized, if the build plate heated via induction heating [6,19]. When using the EBM process, it is possible to preheat the substrate and reheat each powder layer by the defocused electron beam thus minimizing the residual stress significantly, which, represents a clear advantage, in particular for the refractory materials [20–33].

This contribution presents the results of the investigations of pure tungsten fabricated by electron beam melting. At first, the manufacturing process of the tungsten parts by W-EBM, and the results of mechanical tests and microstructural investigations are described. The second section focuses the production of copper cooling structures by means of melt infiltration or selective laser melting (SLM) and on the subsequent manufacturing process of three different mock-ups (W armour and Cu cooling structure) including their computational fluid dynamic (CFD) calculations. The high heat flux testing section describes a first test on tungsten samples with the electron beam facility JUDITH 2 (**JU**elich **DI**vertor **T**est facility located in **H**ot cells) at Forschungszentrum Juelich followed by a second test campaign of the three different mock-ups into the neutral beam facility GLADIS (**G**arching **LA**rge **DI**vertor **S**ample test facility) at IPP Garching. Finally, the results of the postmortem analysis were discussed and suggestions for further investigations are made.

Experimental methods

Tungsten powder characteristics

Tungsten powder produced by gas atomization was received from Tekna (formerly Heraeus Additive Manufacturing, Hanau, Germany). The morphology of the atomized powder particles is highly spherical (important for flowability and raking homogeneous powder layers, see Fig. 1) and the particle size distribution is in ranges between 45 and 90 μm (d10 = 49 μm, d50 = 69 μm, d90 = 98 μm). The chemical purity amounts to 99.9 wt-% with a very low oxygen content of 0.005 wt-% and good flowability.

The powder was stored in a sealed inert environment and after that kept in the vacuum environment of the Arcam A2X machine.

Fabrication of tungsten parts via electron beam melting

The Arcam EBM A2X machine from GE Additive (formerly Arcam AB) is equipped with a high-power electron beam (3000 W) and operates in vacuum (10^{-4} – 10^{-5} mbar) which provides a clean and controlled environment. This is important for the processing of tungsten powder with its high oxygen affinity. The electrostatic charging, the so-called "smoke" was prevented by applying a marginal helium pressure of 10^{-3} mbar. Parts were printed layer-by-layer. The layer information is based on CAD data sliced into layers of constant thickness of 50 μm. For each layer, the electron beam heats the powder to an optimal process temperature and acts as the heat source for pre-heating, re-heating, and melting. The built volume of the A2X unit is 200 mm x 200 mm x 380

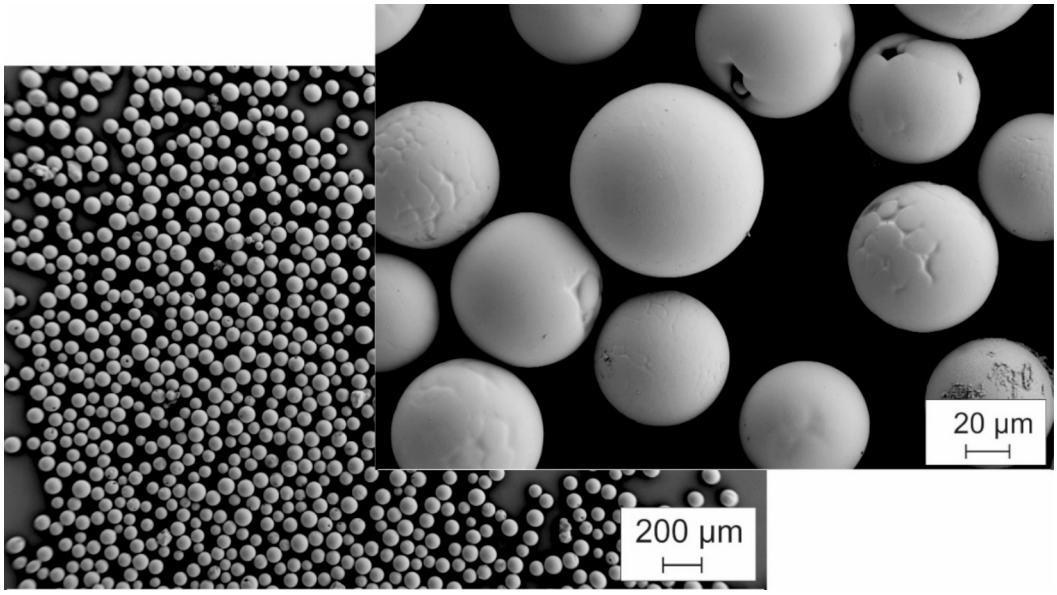

Fig. 1. SEM image of the used tungsten powder.

mm (width x depth x height). Fig. 2 shows a schematic sketch of a generic EBM system. The electrons are emitted by a tungsten filament. The deflection of the beam is controlled by electromagnetic lenses. The vacuum chamber contains the powder in the powder hoppers.

EBM is a powder bed additive manufacturing process. During the build process, the metal powder is fed from the hoppers and the rake fetches powder from each side to generate an even layer on the building platform. A thin layer of powder is distributed, heated, and selectively melted. After melting the layer, the building platform is lowered, and the sequence is repeated until the part is completely built. Fig. 3 shows the main process steps. EBM is an extremely hot process: pre-heating and re-heating eliminate residual stress. Therefore, the EBM build temperatures avoid the formation of cracks [22].

Different techniques have been developed to improve the control of the EBM process. Fig. 4 shows different patterns for heating and melting. The heating step (Fig. 4a) for pre-heating and re-heating eliminates residual stress. This acts as quasi-multi-beam scanning of the total building area with a defocused beam. After pre-heating, the powder surface, the material is melted (powder sintering) within the melting step. Two strategies can be used: hatching or quasi-multi-beam. For melting by hatching the beam goes in lines from left to right or from top to down (Fig. 4b). For melting by quasi-multi-beam, the beam jumps from point to point (Fig. 4c) from outside to inside or the other way, i.e. from inside to outside.

Power and focus of the electron beam are generally determined by the choice of beam current and focus offset, respectively. In order to improve the printing results of this study, it was first necessary to optimize the support structures. These support structures make it possible to dissipate the heat introduced during printing in a targeted manner and to detach the component from the base plate after the printing process. These support structures are also used for so-called overhangs on component geometries. If the support structure is unstable, it detaches from the build platform, for example, which led to swelling at the edges of the printed parts (see Fig. 5). Furthermore, edge swelling is also induced by using inappropriate printing strategies. Optimizing the support structure and printing parameters ensured that the edges of the parts did not swell, resulting in defect-free cubes.

Before printing, the process chamber was evacuated and the building plate was heated up to 1000 °C with a defocused electron beam. The manufacturing of the tungsten parts was carried out by using multibeam

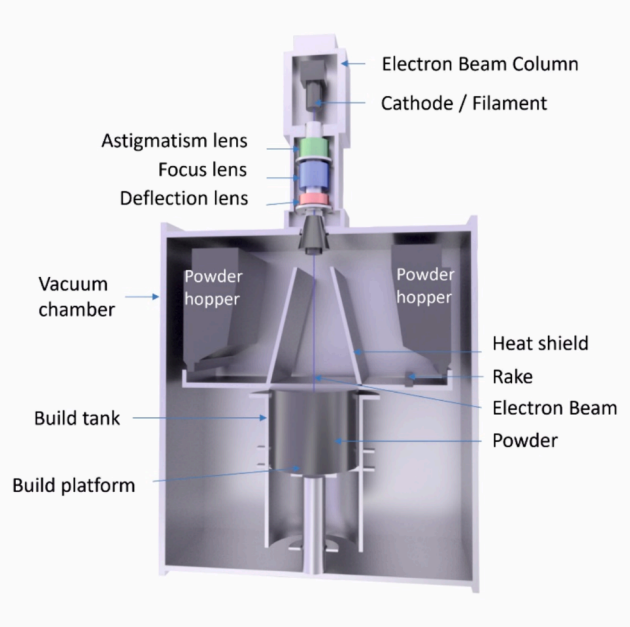

Fig. 2. Schematic sketch of an EBM system according to [24].

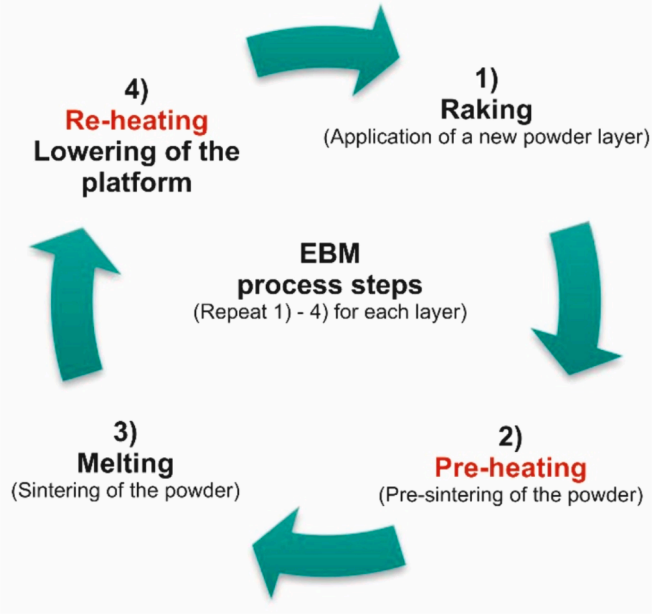

Fig. 3. The main steps EBM processing.

process control with developed process parameters, which comprise a layer thickness of 50 µm, a beam speed of 225 mm/s, a beam current of 14 mA, and a focus offset of 10 mA. Fig. 6 shows printed tungsten samples in various designs after removal from the built platform.

Tensile test samples were printed following three different build directions: standing, laying, and sideward (see Fig. 7). The motivation behind these different directions is to test the impact of the building direction on the mechanical behavior. The nominal dimensions of the samples are: length L = 35.0 mm, width W = 10.0 mm, thickness B = 1.0 mm.

Small-scale Charpy-V impact test specimens (see Fig. 8) were also printed in three different build directions: standing, laying, and sideward. The nominal dimensions of the so-called Kleinstprobe (KLST) small samples are as follows: length L = 27 mm, width W = 4 mm, thickness B = 3 mm, notch depth N = 1 mm, notch angle 60°, notch root radius 0.1 mm. The notch was inserted via electro-discharge machining (EDM) after printing the basic bar geometry.

Characterization and testing methods

Microstructure and crystallographic texture

In preparation for the electron backscatter diffraction (EBSD) measurements, the EBM-printed W armor was sectioned using EDM, whereby the EBM tungsten was probed in the as-printed condition and after high heat flux testing in the GLADIS (Garching LArge DIvertor Sample test facility) neutral beam test facility at IPP, Garching. As a reference, a rolled W plate (produced by Plansee, Austria) with technical purity was studied. The thickness of this commercial W plate was 5 mm. The EDM sections of the EBM W and rolled W were embedded in a hard compound prior to the grinding procedure. Information about the orientation of the cross-sections regarding the mock-up coordinate system is provided later in this paper. The layer presumably affected by EDM was removed by careful grinding. Due to mechanical and subsequent electrochemical polishing, the induced deformation layer was removed. For electrochemical polishing a freshly-prepared etching agent containing demineralized H_2O and 0.66 wt-% NaOH (diluted ASTM electrolyte VII-7 [26]) was set up. We applied a voltage of 10 V activated in intervals of 5 s current and 10 s time-out for 36 cycles, i.e. for a gross duration of 9 min. During the 10 s lasting time-out phases, the sample surface was rinsed with demineralized H_2O.

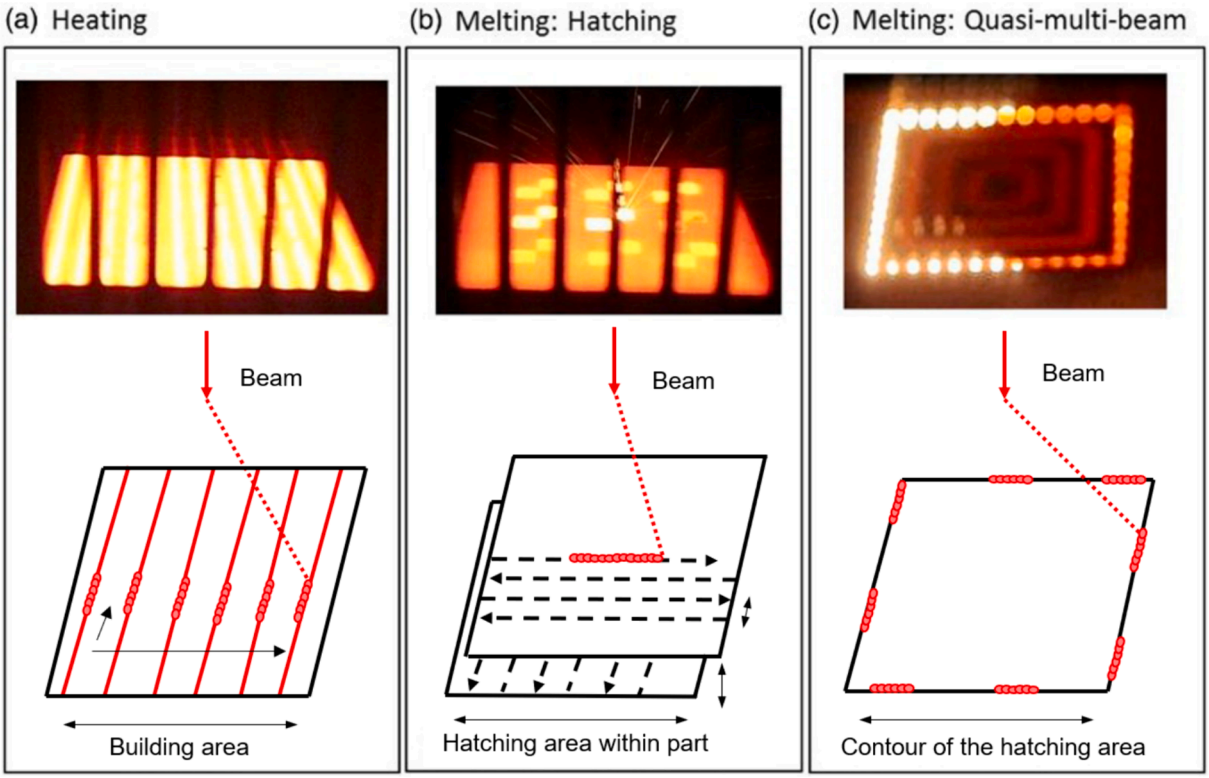

Fig. 4. Heating (a), melting via hatching (b), and melting via multi-beam (c) during the EBM process. Top. photograph during processing, below. schematic sketch of the beam trace according to [25].

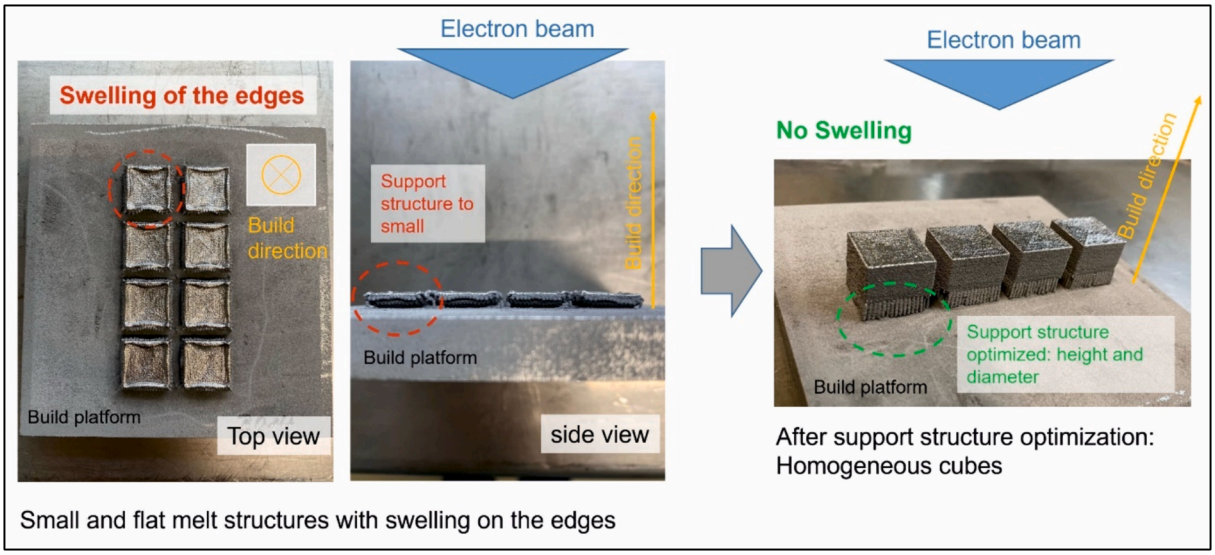

Fig. 5. Optimization of the support structure. inappropriate support structures lead to swelling effects at the part geometry.

Electron backscatter patterns (EBSP) were collected with a high-resolution field emission SEM Merlin (Carl Zeiss, Germany) equipped with a data collection EBSD system Hikari XP (EDAX Inc., USA). The acquisition software utilized was TEAM v4.6 (EDAX Inc., USA). The EBSD camera was operated with 5 x 5 pixel^2 binning and an EBSP acquisition rate of around 300 fps. For scanning the coarse EBM structures the acceleration voltage was 30 kV and the probe current was 20nA. The step size was set to be 5.0 μm at a working distance of 14 mm. To probe the EBM printed samples the combo scan function of TEAM was utilized, i.e. partial areas measuring 950 x 750 μm^2 were collected and finally stitched to generate a single map depicting the complete cross-section. The Plansee rolled plate was scanned with a reduced step size of 0.050 μm collecting a single map with the size 95 x 75 μm^2. The collected area was located at the centerline regarding the normal direction of the rolled plate. Reflecting the much finer grid, the acceleration voltage was adjusted to 20 kV. The further scan parameters remained unchanged to the above-mentioned values of the W-EBM scanning campaign.

By using TSL OIM analysis v8.6, pixels with a confidence index (CI) below 0.1 were eliminated during post-processing. Apart from a grain CI

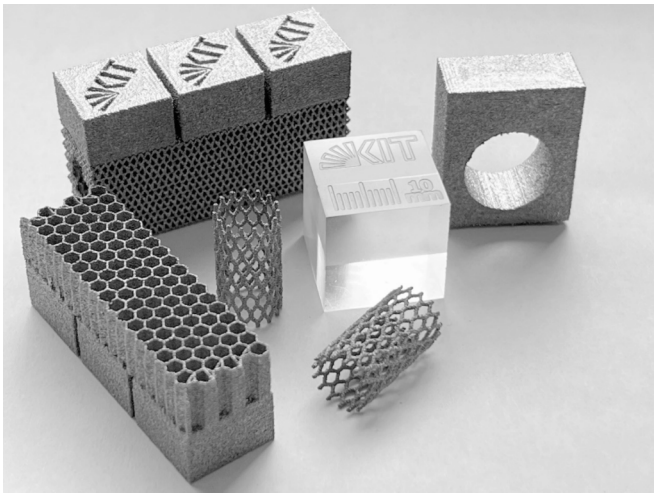

Fig. 6. Differently shaped tungsten samples printed via EBM.

standardization, no clean-up routine was performed on the datasets so that the measured orientation of all the points remained unchanged. In this paper, maps utilizing the color-coded inverse pole figure scheme refers to the crystallographic direction parallel to the building direction (EBM tungsten) and rolling direction (Plansee plate), respectively.

Thermal diffusivity measurements

The high thermal conductivity of 174 W/(m*K) at room temperature [27] is one of the main reasons for the consideration of tungsten as a plasma-facing material (PFM) in nuclear fusion reactors. For the thermal diffusivity measurements, the laser flash method device (LFA 427, Netzsch, Germany) was used for measurements at temperatures between room temperature and 800 °C. A short laser pulse is directed onto the front of a cylindrical sample. The temperature increase is measured as a function of time by an infrared detector. The thermal diffusivity (α) was calculated using the sample thickness (d) and the so-called half max time ($t_{0.5}$):

$$\alpha = 0.1388 \bullet \frac{d^2}{t_{0.5}} \quad (1)$$

Thermal conductivity

The specific heat capacity (c_p) was measured using a differential scanning calorimeter (DSC 204 F1 Phoenix, Netzsch, Germany) at temperatures between −20 °C and 410 °C. The measurements were performed with a heating rate of 10 K/min in argon atmosphere with a flow rate of 50 ml/min. Synthetic sapphire was used as the reference material. The specimens were cut into pieces with 5 mm diameters and 0.5 mm thicknesses. The uncertainty of the specific heat capacity was estimated to be ± 2 %.

The thermal conductivity (λ) was calculated using the measured thermal diffusivity (α), specific heat capacity (c_p) at constant pressure, and the measured density (ρ) of the sample:

$$\lambda = \alpha \cdot c_p \cdot \rho \quad (2)$$

The density of the EBM tungsten samples was measured by the Archimedes method. The sample was weighed in air (m_{air}) and in

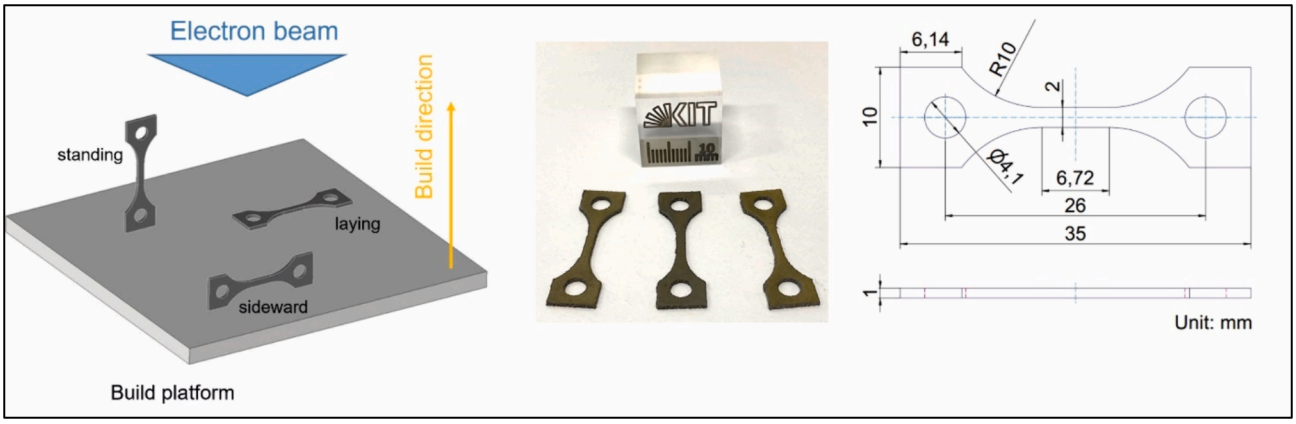

Fig. 7. Fabrication of tensile samples. Left. layout of the build direction on the built platform, middle. finished samples, right. sketch of the used tensile samples.

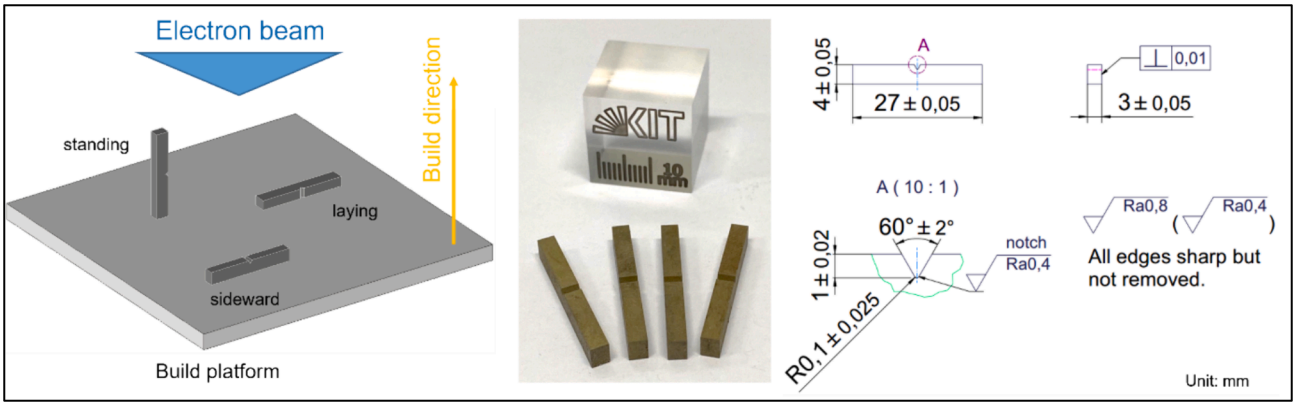

Fig. 8. Fabrication of KLST Charpy-V impact test samples. Left. layout of the build direction on the built platform, middle. finished samples, right. sketch of the used KLST samples.

ethanol ($m_{ethanol}$). The density was then calculated from the two weight as follows:

$$\rho = \frac{m_{air}}{m_{air-m_{ethanol}}} \bullet \rho_{ethanol} \quad (3)$$

where $\rho_{ethanol}$ is the density of high-purity ethanol (0.789 g/cm^3) at RT

Tensile test

Tensile tests were performed by using a general-purpose test frame Z100 (Zwick, Germany) equipped with a high-temperature radiation furnace (Maytec, Germany) at three temperatures (600 °C, 800 °C and 1000 °C) in vacuum (10^{-4} mbar or better) at a constant strain rate of 1 x 10^{-3} s^{-1}. The load–displacement data were converted into engineering stress–strain data.

Charpy impact test

Instrumented Charpy impact tests on KLST specimen (which are based on the EU standard DIN EN ISO 14556:2017–05 [28]) were performed at temperatures between 800 °C and 1100 °C in vacuum (10^{-2} mbar). The maximum impact energy of the used drop-weight machine is 22.6 J, the drop height is 754 mm, the hammer bearing strength is 30 N, and the span of the anvil is 22 mm. All KLST Charpy V-specimen were notched. The absorbed energies were evaluated from the instrumented test data, i.e., from the force–time curves.

Thermal shock test

At Forschungszentrum Juelich, Germany thermal shock tests with the electron beam facility JUDITH 2 (**JU**elich **DI**vertor **T**est facility located in **H**ot cells) were performed with hot water-cooling (T_{in} = 70 °C, P_{in} = 24 bar, v = 25 m/s) [29]. The testing conditions for these high pulse number tests are follows: 105 pulses of 0.48 ms duration time and an intensity from Labs = 0.14 GW/m^2 (FHF = 3 MWs$^{1/2}$/m^2) up to Labs = 0.55 GW/m^2 (FHF = 12 MWs$^{1/2}$/m^2) with a repetition frequency of 25 Hz. A base temperature of 700 °C (homogeneous surface temperature) was achieved by using a (quasi) steady-state heat load of 10 MW/m^2. For the experiments, three W-EBM bulk samples with a size of 15 x 15 x 5 mm^3 were ground and mirror-like polished from each surface.

High heat flux test

The **G**arching **LA**rge **DI**vertor **S**ample test facility (GLADIS) at IPP Garching, Germany serves to investigate the thermo-mechanical behavior of components subjected to extreme thermal loads comparable to the plasma conditions in the divertor. The facility is equipped with two 1 MW neutral beam sources for homogeneous heating of plasma-facing components at heat fluxes up to 45 MW/m^2 and 45 s pulse length [30]. The aims of the High Heat Flux (HHF) tests of pure W-EBM mock-ups were: (1) to study the thermo-mechanical behavior (temporally-resolved surface temperature evolution during screen and cycling) and (2) to study changes in surface morphology due to the high temperature and high heat flux (grain growth, porosity, surface structure).

Results and discussion

Microstructure and crystallographic texture

Electron backscatter diffraction (EBSD) is a powerful microstructural characterization tool. Fig. 9 shows the crystallographic directions in building direction for EBM tungsten exemplary on a fabricated monoblock geometry. A typical columnar grain structure formed along the built direction is clearly visible presumably due to the printing process. This epitaxial grain growth is parallel to the direction of the maximum temperature gradient and is also reported in literature [20,21]. The width of the columnar grains is about 50–100 µm. The length of these long columnar structures is between 1 to 5 mm and indicates a stable melt pool during the EBM process [21]. Only a few micropores are found in the EBM tungsten samples, however, no microcracks are visible. The absence of microcracks benefits from the combination of vacuum environment to reduce the oxide impurities (oxygen reacts very fast with tungsten at higher temperatures) and the preheating from the heating schemes above the ductile-to-brittle-temperature (DBTT) of tungsten. At higher temperatures, the dislocations are more mobile, plastic deformation can occur, thus reducing the chance of cracking [22,31]. This demonstrates the superiority of EBM for printing tungsten if compared with SLM pure tungsten samples that contain microcracks and micropores [10,32].

The grain structure toward the building direction is shown in Fig. 10. The presence of just red and blue colors indicates a preferent growth of grains with ⟨100⟩ or ⟨111⟩ direction parallel to the building direction. In this cross-section equiaxed grain morphologies were observed with diameters in the range of 10 to 120 µm.

Fig. 11 shows the crystallographic directions of the reference material (a Plansee rolled tungsten plate with a thickness of 5 mm whereby the IPF color code is referring to the rolling direction. In comparison with the coarse solidification structure of the W-EBM the reference material is very fine-structured and small grains are visible. Frequent greenish-colored grains indicate the presence of an alpha-fiber dominated rolling texture.

Fig. 9. Microstructure along the building direction. Crystallographic direction parallel to the building direction.

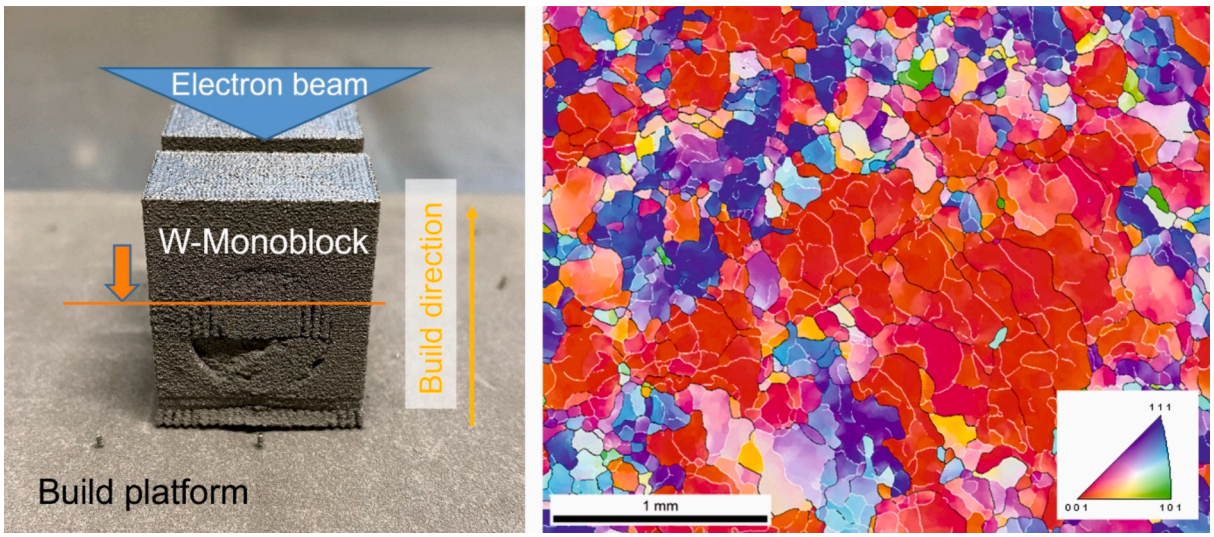

Fig. 10. Microstructure perpendicular to the building direction. Crystallographic direction parallel to the building direction.

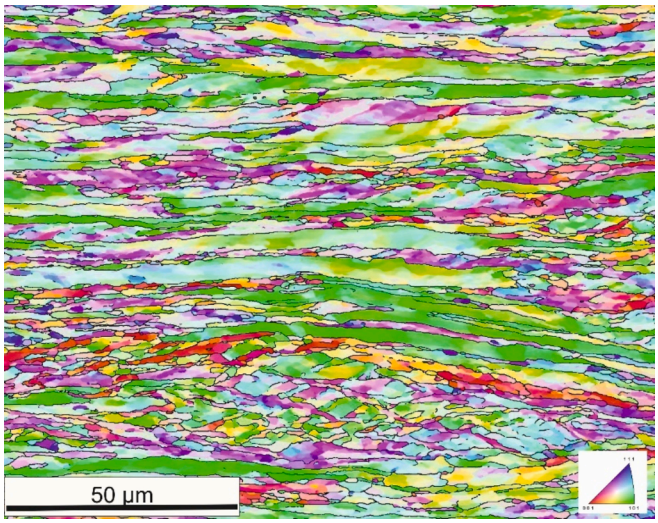

Fig. 11. Crystallographic direction of the reference tungsten (rolled tungsten plate, thickness 5 mm) along the rolling direction.

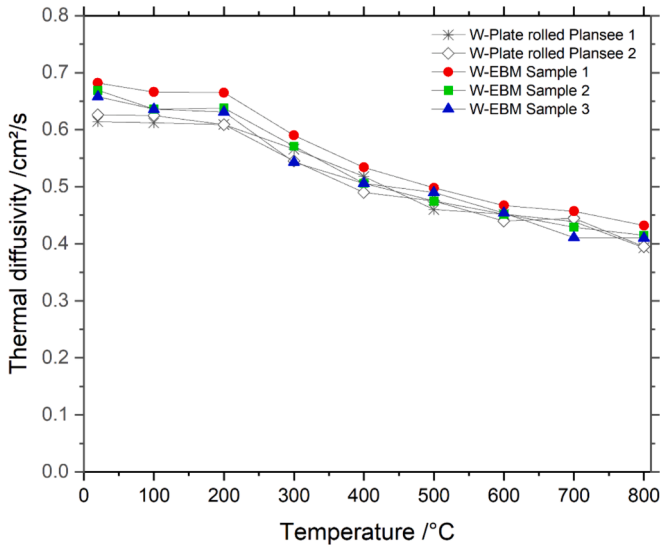

Fig. 12. Thermal diffusivity of tungsten fabricated via EBM and rolled tungsten plate from Plansee. For better visualization the measured data points were linked.

Thermal conductivity and density

Fig. 12 shows the results of thermal diffusivity measurements on three tungsten EBM samples and two rolled tungsten plates produced by Plansee. The thermal diffusivity decreases with increasing temperature due to the phonon scattering. No notable differences between EBM-W and the rolled W plates are visible.

Fig. 13 shows the specific heat capacity measurements. At room temperature, the specific heat capacity of EBM tungsten is 0.130 J/(g*K), (literature [1]: 0.133 J/(g*K)) and the measured values increase with increasing temperature.

The thermal conductivity of commercial tungsten (density: 19.25 g/cm^3) is 174 W/(m*K) at room temperature [34], and the measured thermal conductivity of EBM tungsten (density: 19.21 g/cm^3) is 165.42 W/(m*K). The thermal conductivity decreases with the increase of the test temperature due to the dominating effect of the thermal diffusivity (see Fig. 14).

Mechanical properties

Tensile testing

Tensile tests were carried out at three temperatures: 600 °C, 800 °C, and 1000 °C. The related stress–strain curves are shown in Fig. 15.

The total elongation for the laying and sideward samples is in a range of 20 % and 30 %, respectively. For the standing samples, total elongations between 70 % (600 °C) and 80 % (1000 °C) were achieved. Since the grain size parallel to the printing direction is several mm, we assume some kind of single crystal tensile behaviour. Compare to the polycrystaline tungsten, single crystal show higher ductility even at lower test temperature [35]. The samples sidewards and laying orientation do not show this high tensile ductility, since the high angle grain boundaries are 90° oriented to the tensile direction. High angle grain boundaries in tungsten are prone to brittle behaviour [2]. As shown in Fig. 16, the standing specimens exhibit significant necking across all test temperatures. The fracture surface (see Fig. 17) exhibited macroscopic features of plastic deformation. The sideward and laying specimen, tested at 600 °C, failed in a brittle manner without necking. At 1000 °C

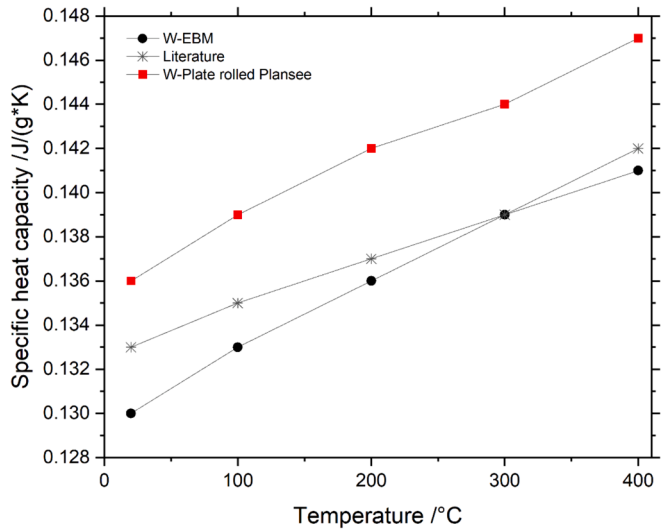

Fig. 13. Specific heat capacities of EBM tungsten and rolled Tungsten (Plansee) vs. Literature (Touloukian [33]).

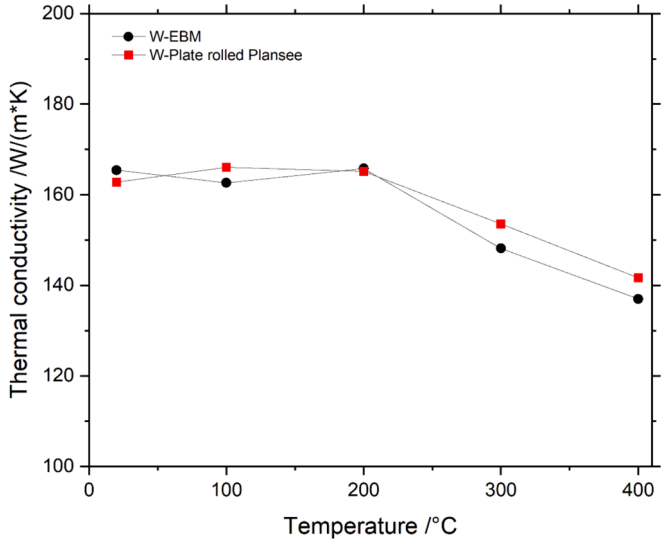

Fig. 14. Thermal conductivity of EBM tungsten and a rolled tungsten plate (Plansee).

these printing directions show slight necking and fine secondary cracks. The fracture mode appears to be a mixed type comprising cleavage and intergranular fracture. In contrast, the standing specimens tested from 600 to 1000 °C show strong necking with coarse secondary cracks of the fracture surface. The fracture mode of the standing samples is transgranular at all three test temperatures.

Consequently, we can conclude that the building direction significantly influences the properties of the EBM-printed tensile samples – and thus also the behavior of later components. This must be taken into account with regard to the later functional use of an EBM printed component.

Fig. 18 compares the tensile testing curves of the rolled tungsten plate and EBM-printed tungsten (standing orientation). Rolled tungsten shows a much higher strength but a significantly lower uniform and total elongation. With 80 % to 90 % the total elongation in build-direction of EBM-printed tungsten is extraordinarily high for tungsten. However, yield strength and UTS are lower than observed for rolled tungsten.

Charpy impact testing

In Fig. 19, the Charpy energy is shown for the test temperatures 800 °C, 1000 °C and 1100 °C. The notched (KLST) samples made of sideward and laying printed EBM tungsten failed in a brittle manner even at 1100 °C. In contrast to that, the standing printed samples show a significant increase in Charpy energy at 1000 °C (6.5 J) and at 1100 °C (7.1 J). The DBTT of the standing specimens is in the range as observed with the Plansee plates.

Typical appearances of specimens after the Charpy impact tests at temperatures between 800 and 1100 °C are shown in Fig. 20. The specimen printed sideward and laying fractured in a brittle mode, i.e. material separation without lateral extension. The specimens printed in standing orientation show for all three testing temperatures plastic deformation and ductile behavior in the case of 1100 °C. A similar behavior can be observed for the rolled tungsten plates, which were used as a reference.

Thermal shock testing at JUDITH 2

Fig. 21 shows the SEM images of the surfaces and cross sections of the three W-EBM samples after testing for 10^5 pulses at increasing transient heat load power densities. With higher intensity, the tungsten surfaces deteriorate due to surface roughening and cracking. Despite this, no deterioration of power handling capabilities or overheating took place. Furthermore, no clear sign of macroscopic cracking was observed after 10^5 pulses of up to 12 $MWs^{1/2}/m^2$ at 700 °C.

Divertor target mock-ups: Design and fabrication

As shown in Fig. 6, the EBM process allows the production of tungsten parts of various geometries. This advantage allows to explore new approaches in the design and manufacturing of divertor targets. While, initially, the introduction of the supporting structure was intended to improve the quality of the printed (massive) tungsten slab, later on it was recognized that, given the good quality of the lattice structure, its presence in the raw EBM product could be useful when connecting the tungsten armor to the cooling structure. Previous studies [19,36] demonstrated successful the combination of tungsten lattice structure samples fabricated via Laser powder bed fusion (LPBF) and melt infiltration with copper. Thus, using this structure as an anchoring element, the massive tungsten part can be limited to the plasma-facing side of the target, while its backside could be made out of the same material as the cooling channel. The concept, also known as a “flat-tile” solution, found limited application in the past mainly due to the issues related to the joining between the tungsten tiles and the heat sink usually made of copper or copper alloys. The presence of the lattice structure in the W-EBM tungsten raw parts can be used to create compliance layers that could mitigate the stresses resulting from the difference between the thermal expansion of copper and tungsten as well as due to the one-sided loading of the target. In this section, we are introducing three new divertor target designs each of them based on tungsten armor produced by an EBM process but featuring different cooling concepts and different methods of connecting the tungsten part to the cooling channel. While the main objective is to characterize the quality of the tungsten armor under fusion-relevant heat loads, having mock-ups with different cooling schemes and manufacturing steps give us a first indication of their behaviour during high heat flux tests. By studying the thermo-mechanical behavior (temporally-resolved surface temperature evolution during screen and cycling) and the surface morphology changes due to high temperature and high heat fluxes (grain growth, porosity, surface structure). In addition to that, a special interest concerns the investigation of the potentials and the pitfalls of the different manufacturing procedures as well as the performances of the three selected cooling solutions.

High heat flux (HHF) testing was performed in the GLADIS test facility at IPP Garching. This facility serves to investigate the thermo-

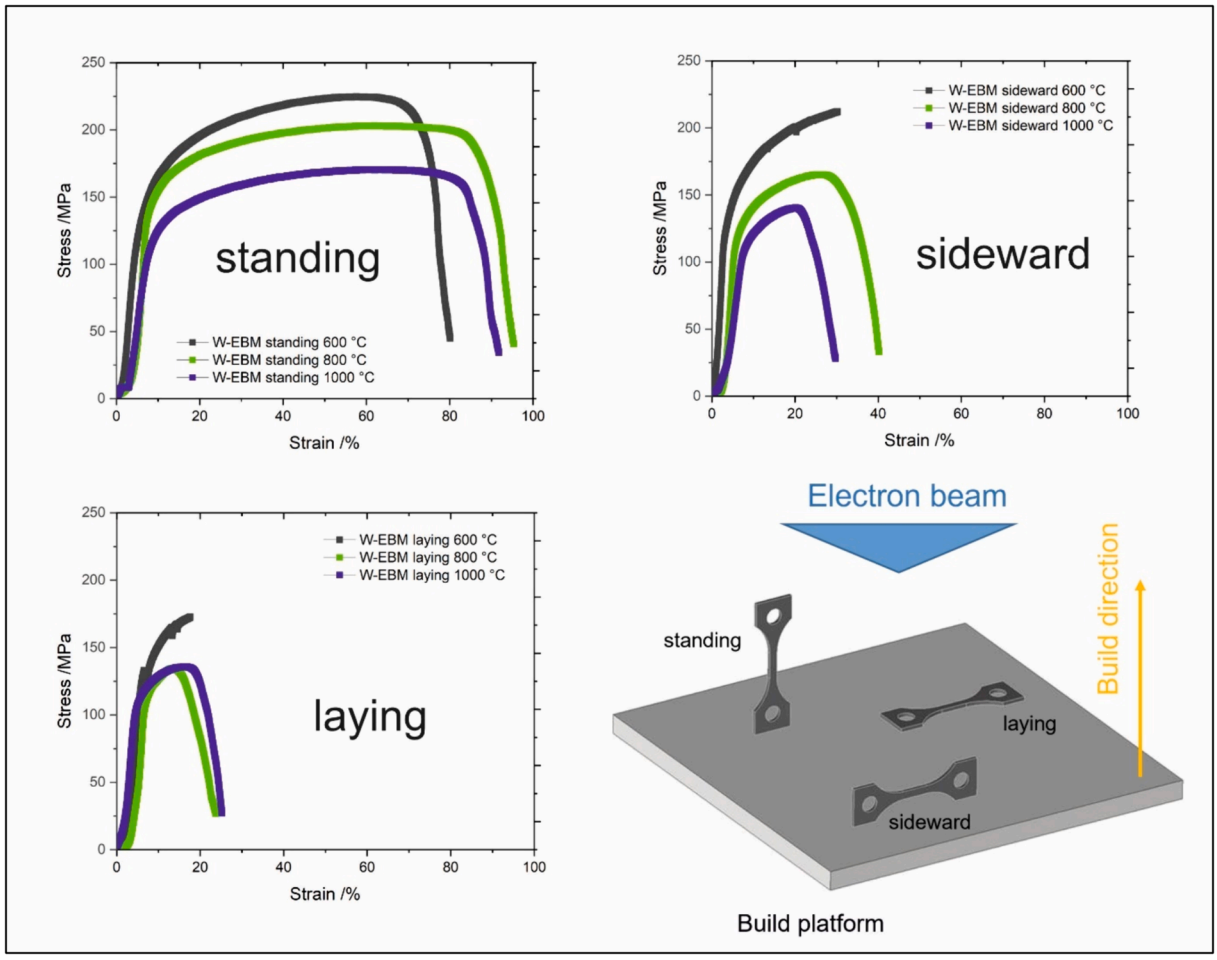

Fig. 15. Tensile test results of EBM tungsten. Note. Total elongation scatters about ± 20 % between several tests.

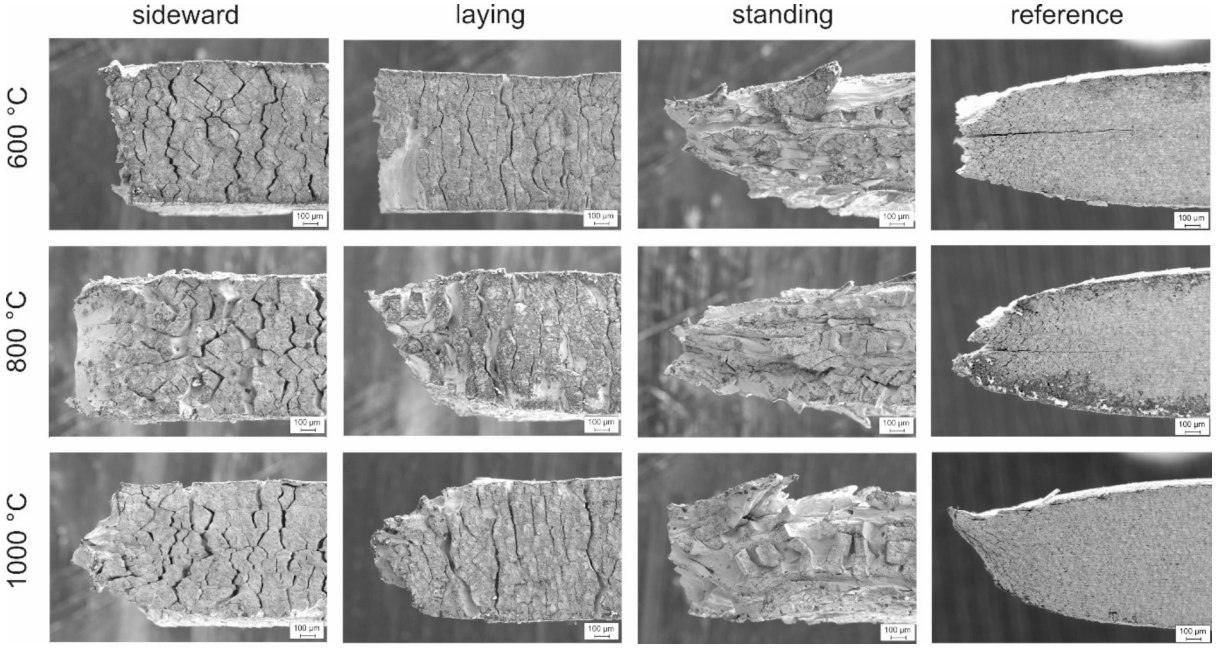

Fig. 16. SEM images of the W-EBM specimens (side view) after tensile testing. Reference. Plansee tungsten plate tested in rolling direction.

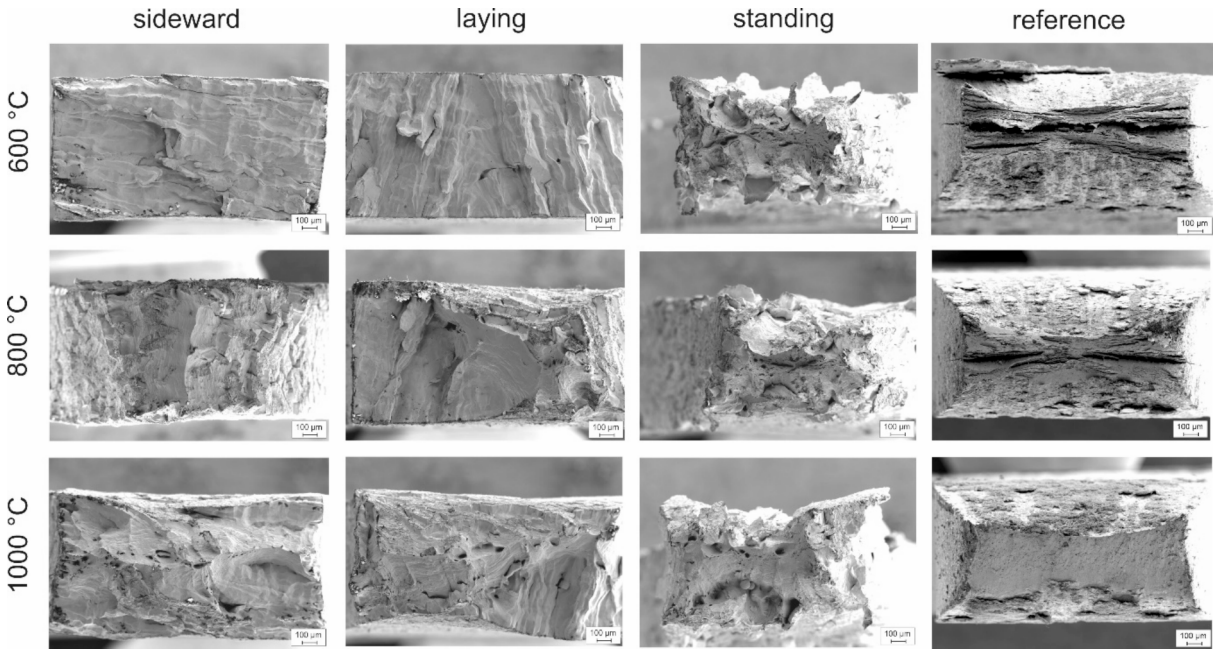

Fig. 17. SEM images of the W-EBM specimens (fracture surface) after tensile testing. Reference. Plansee tungsten plate tested in rolling direction.

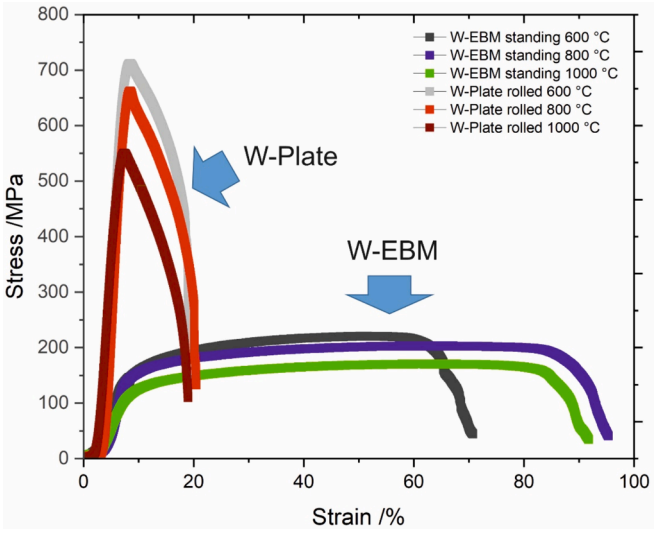

Fig. 18. Tensile test results. W-EBM (standing orientation) vs. rolled W-plate as reference (sample removal in rolling direction). Note. Total elongation scatters about ± 20 % between several tests.

mechanical behavior of divertor components subjected to extreme thermal loads.

While one of the mock-ups follows more or less the current baseline (tungsten slab cooled by a swirl flow), the other two mock-ups explore the possibility of implementing more complex cooling concepts by using additive manufacturing techniques for the heat sink channel. Because, at the time of the parts manufacturing, we had access only to cooper-based additive manufacturing techniques (selective laser melting – SLM), all three mock-ups used copper instead of copper-chrome-zirconium (CuCrZr) which is the selected material for the baseline solution.

Fig. 22 gives an overview of the processing routes for the different design types of the mock-ups. Common to all mock-up designs is the fabrication procedure of the parts via W-EBM. In all three cases, the flat-tiles consist of a massive part acting as divertor armor built on a lattice structure. The second step of the manufacturing process is also similar for the three mock-ups, the grid being melt infiltrated with pure Copper. From this point on, the fabrication process follows different paths:

- Mock-up I: Combination of W-EBM and Cu-Infiltration – w/o additional joining.
- Mock-up II: Combination of W-EBM and Cu-SLM – joining via brazing.
- Mock-up III: Combination of W-EBM and Cu-SLM – w/o additional joining.

Cooling concept and fabrication route of mock-up I

For the first mock-up, whose design was motivated to avoid a joining/brazing between the W-EBM part and the heat sink the implementation of the swirl cooling concept (similar to the baseline solution) was rather straightforward. Fig. 23 shows the geometric details of mock-up I. The armor structure consists of three tungsten tiles in cube design each 14.5 mm x 14.5 mm (length x width) with a height of 8.3 mm. The distance between the tiles is 1 mm. After printing the W tile grid structure via W-EBM, the W grid was melt infiltrated with pure copper. For the infiltration process a big box made of stainless steel with a length of 100 mm was used. The assembly was slowly heated-up to 1100 °C, held for 20 min at the temperature and slowly cool-down subsequently, all under vacuum conditions. After Cu infiltration, the copper contour was mechanically machined by turning and milling. The pipe-style cooling channel with a diameter of 10 mm was machined by drilling and a twisted tape with a twist ratio of 2.375 was inserted. Fig. 24 shows the details of the fabrication route and Fig. 25 shows the final state.

The mock-up behavior under high heat flux testing conditions was simulated using ANSYS CFX. For this purpose, the model uses for the water the IAPWS IF97 properties as implemented in CFX. The copper-infiltrated tungsten structure is replaced by a part having a uniform material composition with thermal properties calculated as the properties of a mixture using a volumetric weighting.

The water enters the mock-up at a pressure of 15 bar (a) with a velocity of 12 m/s, having a temperature of 15 °C. Two HHF testing scenarios were considered, one with a peak heat load of 12 MW/m^2 and one with 15 MW/m^2. The applied heat load distribution on the surface is modeled according to the loading profile of GLADIS, and is shown in Fig. 26. Due to the size of the gaps between the tungsten slabs, the model

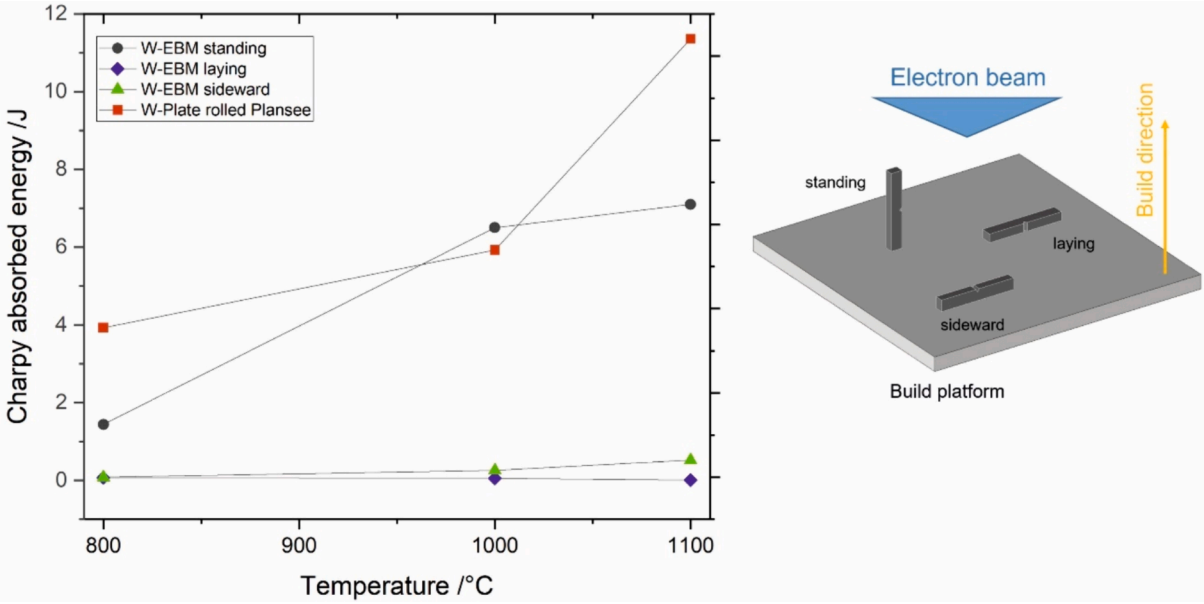

Fig. 19. Results of the Charpy impact tests, all samples notched.

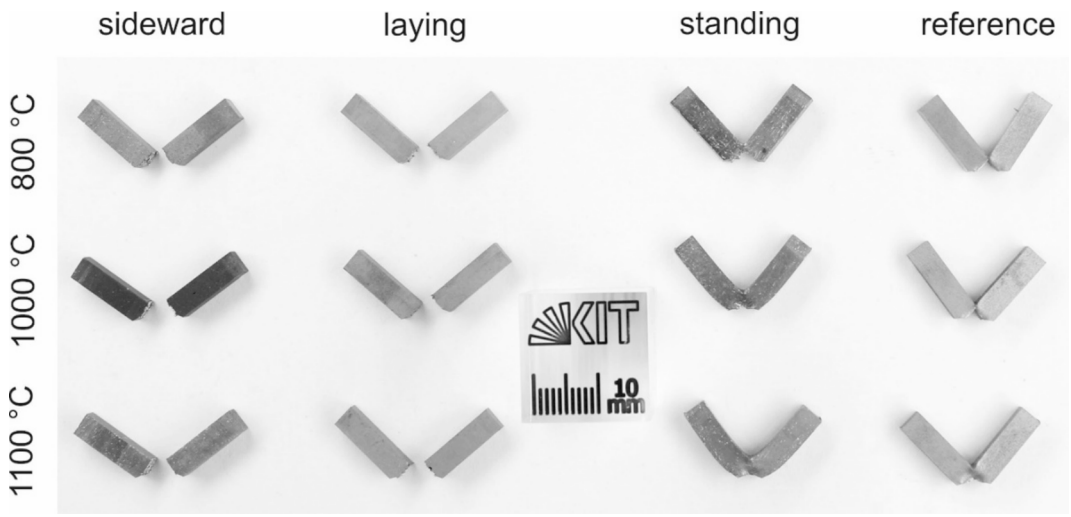

Fig. 20. Appearances of EBM tungsten (sideward, laying, standing) and reference tungsten (rolled plate) specimens after Charpy impact testing.

assumes that the heating is applied also on that particular surface.

The resulting steady-state temperature field during 15 MW/m^2 loading is shown in Fig. 27.

Cooling concept and fabrication route of mock-up II

The second mock-up makes use of a hypervapotron cooling concept, a solution characterized by an efficient heat removal performance during the fully subcooled boiling regime [37]. For this concept, the cooling channel has a rectangular cross-section and the heat-loaded side has fins manufactured perpendicularly to the coolant flow direction. At low heat loads, forced convection is the main heat transfer mechanism. At higher heat fluxes, when the local critical heat flux is exceeded, the liquid between two adjacent fins starts to boil creating a steam bubble between the fins. This steam condenses when in contact with the bulk subcooled flow, allowing cold liquid to rewet the heated surface [37–39]. The solution has critical heat flux values superior to 30 MW/m^2 [40] which is very attractive for divertor applications.

Fig. 28 shows the geometrical details of mock-up II. The armor structure consists of three flat-tiles each 26 mm x 12 mm (length x width) and 11.5 mm in height. The distance between the tiles is 1.2 mm. The cooling channel dimensions adopt a hypervapotron geometry similar to the one investigated by Baxi and Falter [38], having a 22 mm wide channel and 7 mm height; the fins have a 3 mm pitch and a 4 mm height leaving a 3 mm for the bulk flow. Note that, as compared to the previous mock-up, the width of the tungsten slab is larger by almost 80 %, 26 mm compared to 14.5 mm. Since the length of the slabs is slightly smaller (12 mm compared to 14.5 mm), the increase of the loaded surface is only 48 %. This means if tested with the same beam profile as utilized for mock-up I, mock-up II will receive about 50 % more power than mock-up I.

Fig. 29 shows details of the fabrication route of mock-up II. After printing the W flat-tile with grid structure via W-EBM, the W grid was melt infiltrated with pure copper (similar to mock-up I). The W grid Cu contour was mechanically machined. In contrast to mock-up I, the cooling structure made of pure copper was printed via selective laser melting (SLM) on an SLM M280 machine (SLM Solutions, Germany). The used process parameter of this system includes a layer thickness of 50 μm, a laser power of 350 W, a laser scanning velocity of 800 mm/s,

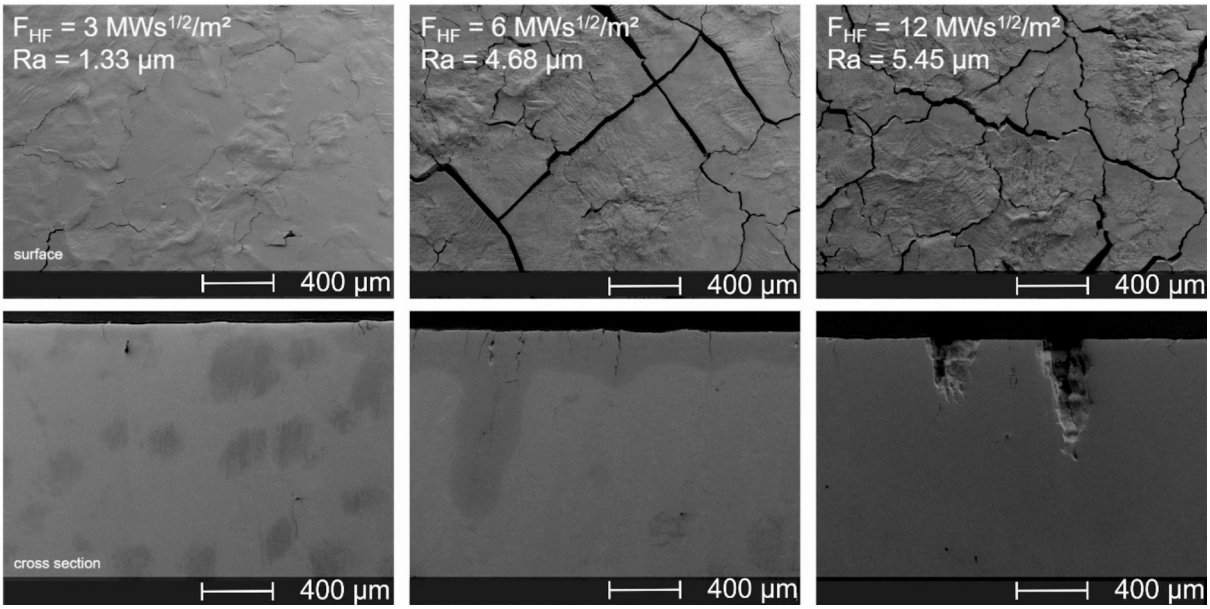

Fig. 21. SEM images of the three W-EBM samples. surfaces (top) and cross sections (bottom) after 10^5 pulses at different transient heat load power densities.

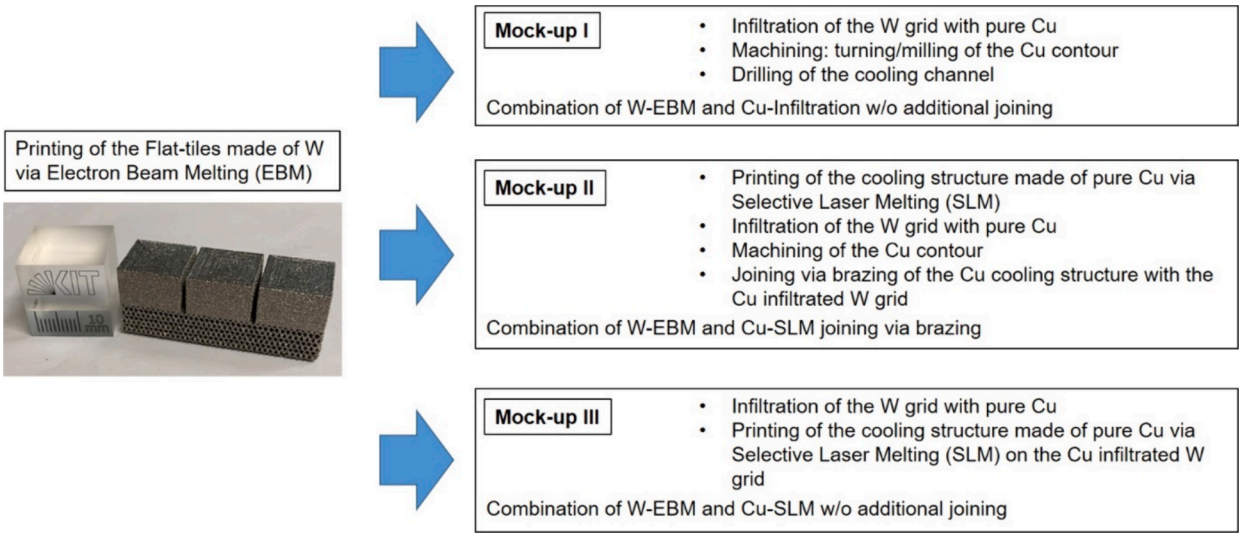

Fig. 22. Processing routes of the three different Mock-ups.

and a hatch distance of 120 µm. A stripes scanning strategy was applied. The starting plate was made of steel and pre-heated to 200 °C. The size of the copper particles (99.9 wt-% purity) was in a range between 20 and 45 µm. The internal structure of the copper cooling component was analyzed via micro computed tomography (µCT), see Fig. 29. The YXLON Precision µCT system was set up with an acceleration voltage of 200 kV at a target current of 0.2 mA with an additional 0.5 mm thick Cu filter for beam hardening reduction. Altogether 1890 projection images were recorded on the Perkin Elmer XRD1620 AN flat panel detector with an integration time of 1000 ms. Three images were averaged for each projection to reduce noise. The detector had a size of 2048 × 2048 pixels and a pixel pitch of 0.2 mm resulting in a final voxel size of 25 µm in the reconstructed volume image. The edges of the cooling channel are clearly visible. Finally, the W flat-tiles with Cu infiltrated grid and the Cu cooling structure were joined via brazing ("Gold braze": 82 wt% Au, 18 wt% Ni, brazing temperature: 980 °C). Fig. 30 shows the produced mock-up in the final state.

Similarly to the first mock-up, the HHF performances were evaluated using an ANSYS CFX model. In this case, the model represents only half of the mock-up, taking advantage of its symmetry. The modeling of copper-infiltrated part is done the same way as for mock-up I, using a volume-weighted average of the individual heat conductivities.

The simulations assume a cooling water with a pressure of 14 bar that enters the connecting tube with a velocity of 8 m/s and a temperature of 16 °C. The surface heat loading conditions are the same as for mock-up I, the beam being centered on the second tungsten slab. Fig. 31 presents the calculated temperature field for the two loadings.

The higher tungsten surface temperature as compared to the first mock-up is mainly due to the (minimum) distance between the tungsten surface to the water cooling is larger in case of Mock-up II (18.65 mm) than in case of Mock-up I (12 mm). In addition to that, Mock-up II has a thicker tungsten block (11.5 mm) as opposed to only 8.3 mm for Mock-up I.

Cooling concept and fabrication route of mock-up III

The third mock-up uses a combination of cooling channel geometry

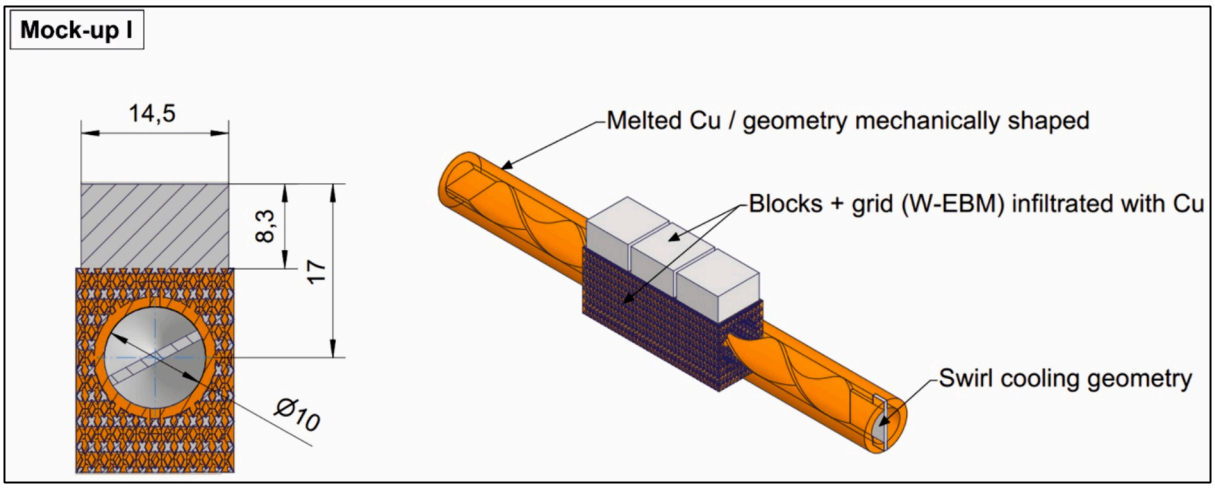

Fig. 23. Details of mock-up I.

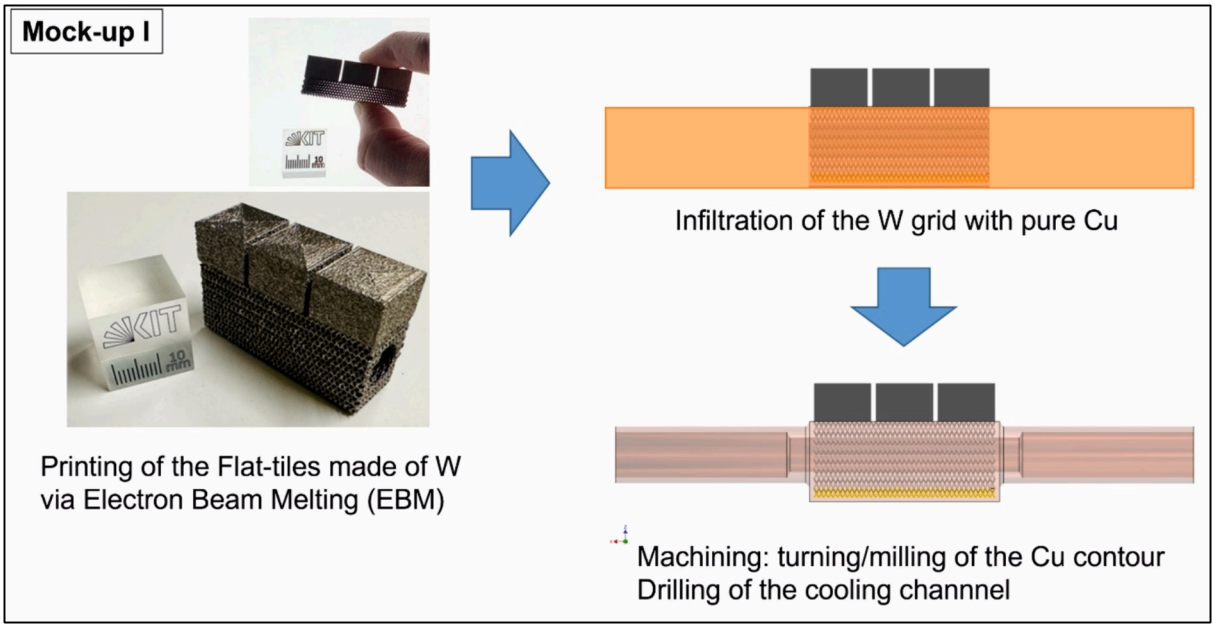

Fig. 24. Processing route of mock-up I.

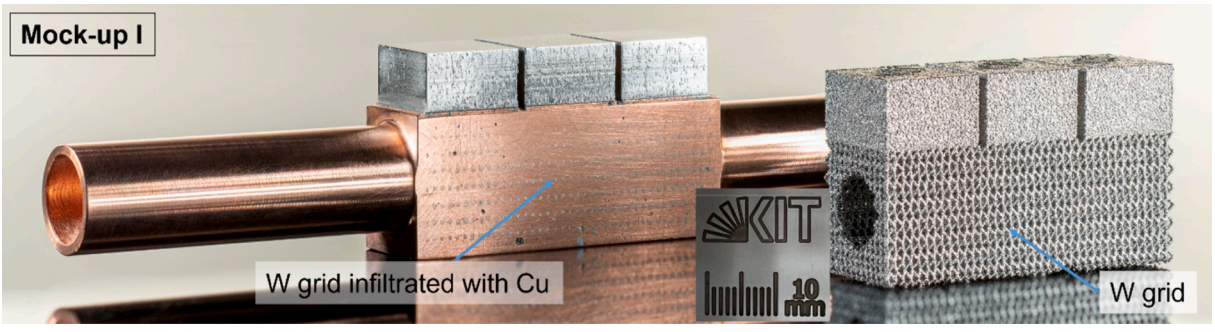

Fig. 25. Mock-up I. Combination of W-EBM and Cu-Infiltration, w/o additional joining. W tile and grid after fabrication via W-EBM (right) and the final state after Cu infiltration and mechanical machining (left).

and turbulence promoters to achieve a high heat transfer. In terms of heat-loaded surface and overall dimensions, this mock-up is the same as the second mock-up. However, the cooling channel cross-section is divided into two flow areas having a quasi-triangular geometry as can be seen in Fig. 32. In addition to that, on the heated-side wall, there are arrows (1 mm in height) acting as turbulence promoters for enhanced

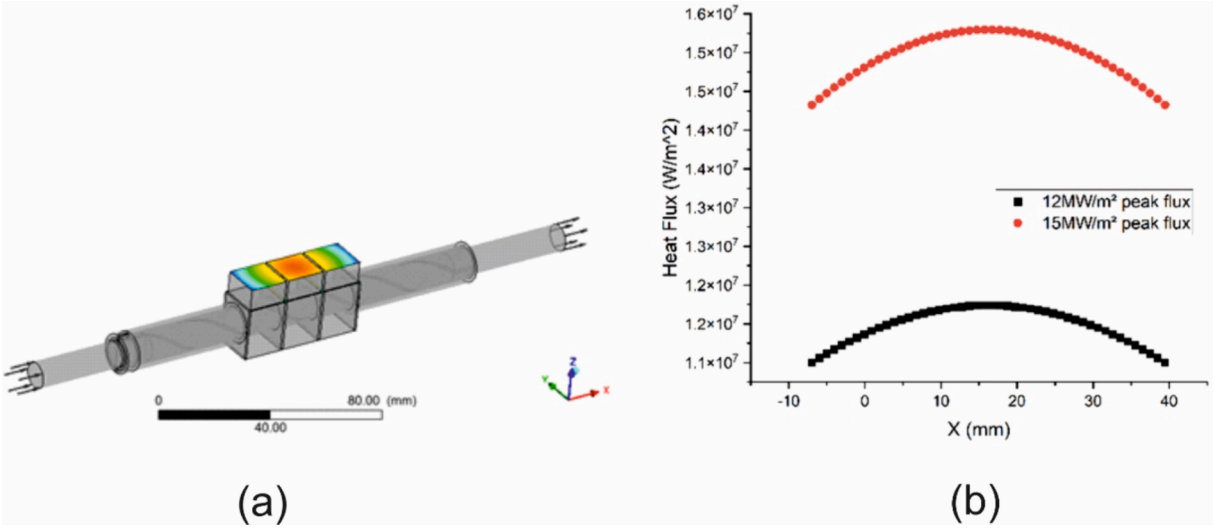

Fig. 26. CFX model of mock-up I with heat flux loading conditions. (a) applied heat flux profile; (b) heating profile along the axial direction for the two simulated cases.

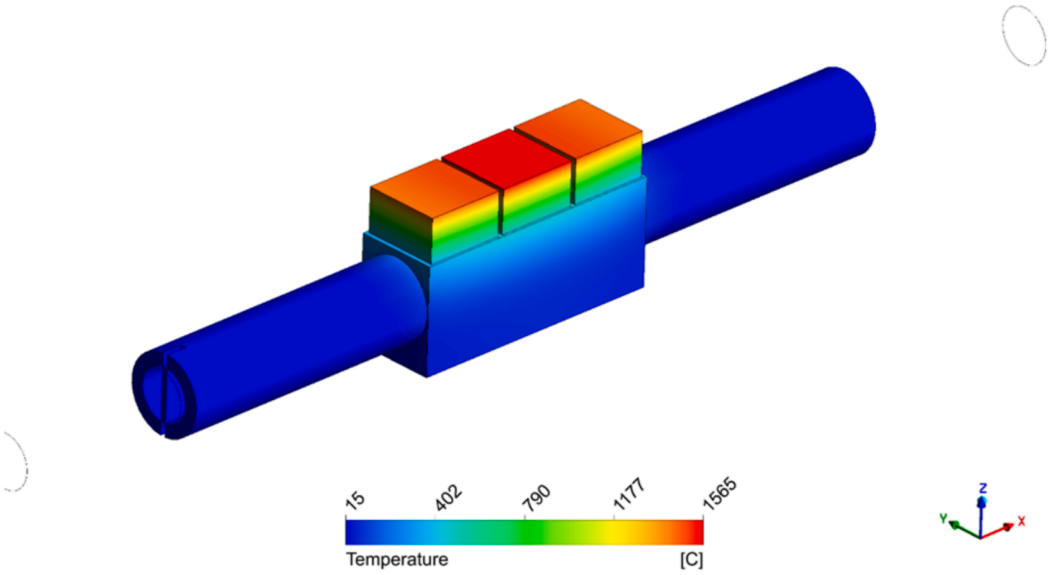

Fig. 27. Mock-up I temperature field for a loading with a 15 MW/m^2 peak heat flux.

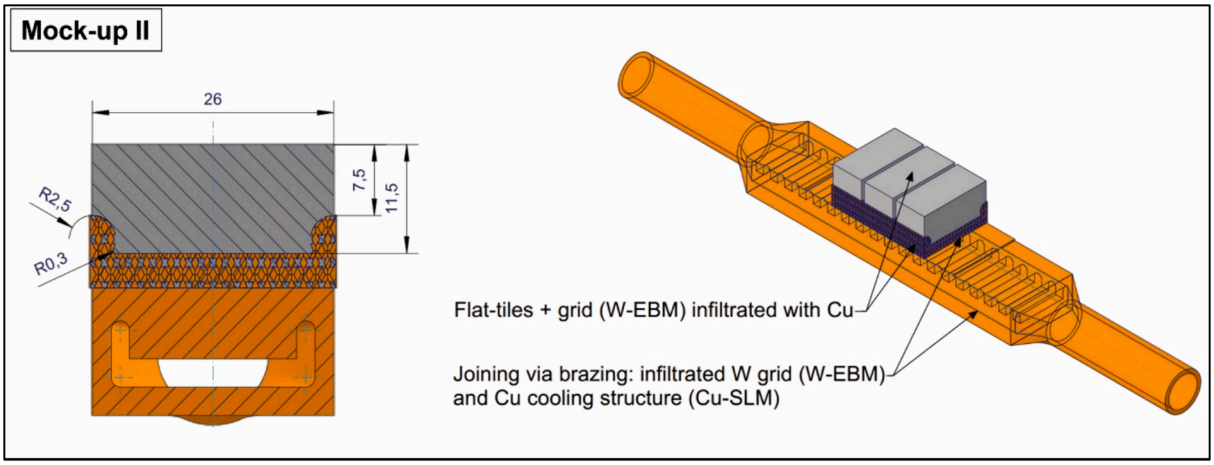

Fig. 28. Geometric details of mock-up II.

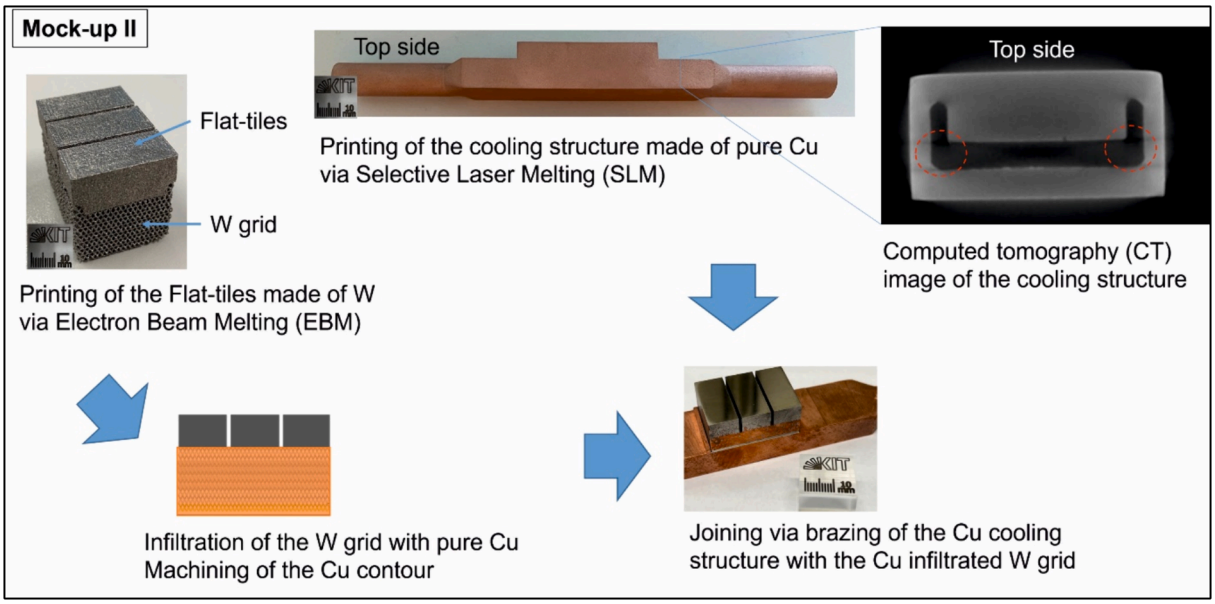

Fig. 29. Processing route of mock-up II.

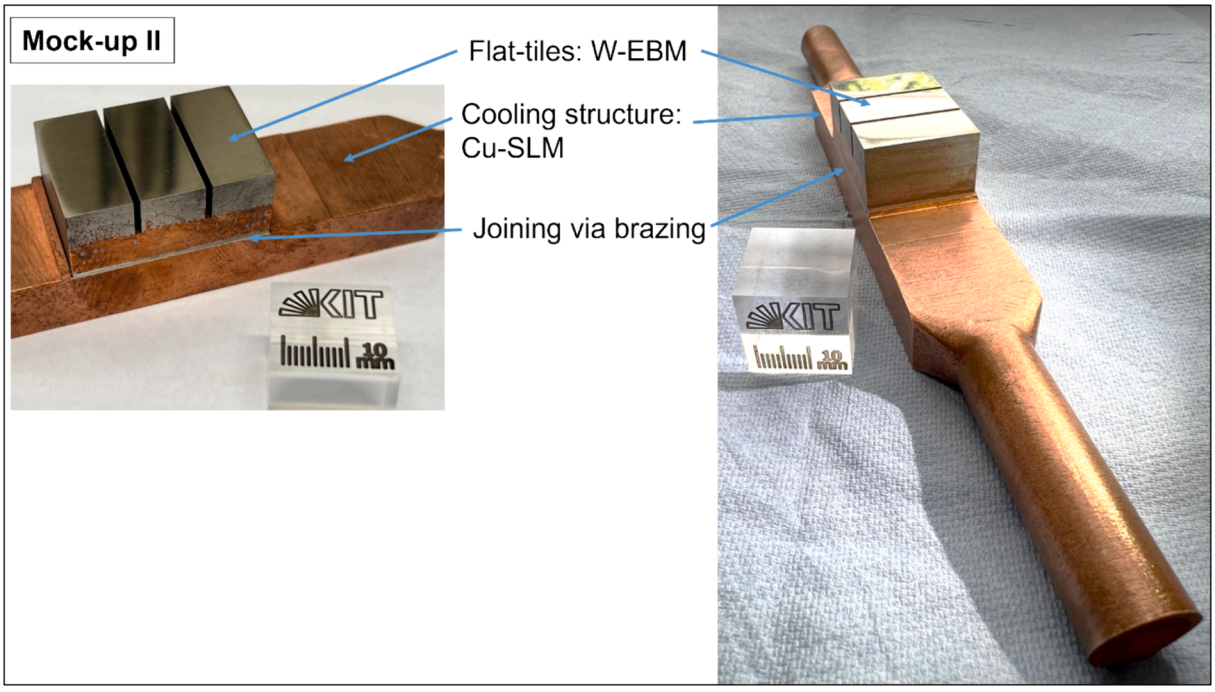

Fig. 30. Mock-up II. Combination of W-EBM and Cu-SLM, joining via brazing.

heat transfer. This combination results in a solution that has better cooling capabilities than the hypervapotron, in terms of the tungsten temperature and the pressure loss.

Fig. 32 shows the geometrical details of mock-up III. The armor structure consists of three flat-tiles each 26 mm x 12 mm and with a height of 11.15 mm. The distance between the tiles is 1.2 mm. The Cu cooling structure was optimized via computational fluid dynamics (CFD).

After printing of the W flat-tile grid structure via W-EBM, the W grid was melt infiltrated with pure copper and the W grid Cu contour was mechanical machined. After this, the prepared structure was flipped and put upside down into the SLM printer. Fig. 33 shows the details of the fabrication route of mock-up III. The cooling structure made of pure copper was printed directly via SLM (the same machine and process parameters as used for mock-up II) on the copper infiltrated and mechanical fixed W grid. Fig. 34 shows the final state after surface polishing.

For this mock-up, both cases, 12 MW/m^2 and 15 MW/m^2 loading are computed (see Fig. 35). The cooling water is assumed to enter the mock-up with a velocity of 8 m/s, under a pressure of 14 bar and a temperature of 16 °C.

If comparing the tungsten temperatures of mock-up II and mock-up III we can see that the values are, in average, 150 °C lower for the latter. This is mainly due to the strong mixing effect associated with the arrows presence. Also, an important fact is the different heights of the flat-tiles (mock-up I: 8.3 mm, mock-up II: 11.5 mm, mock-up III: 11.15

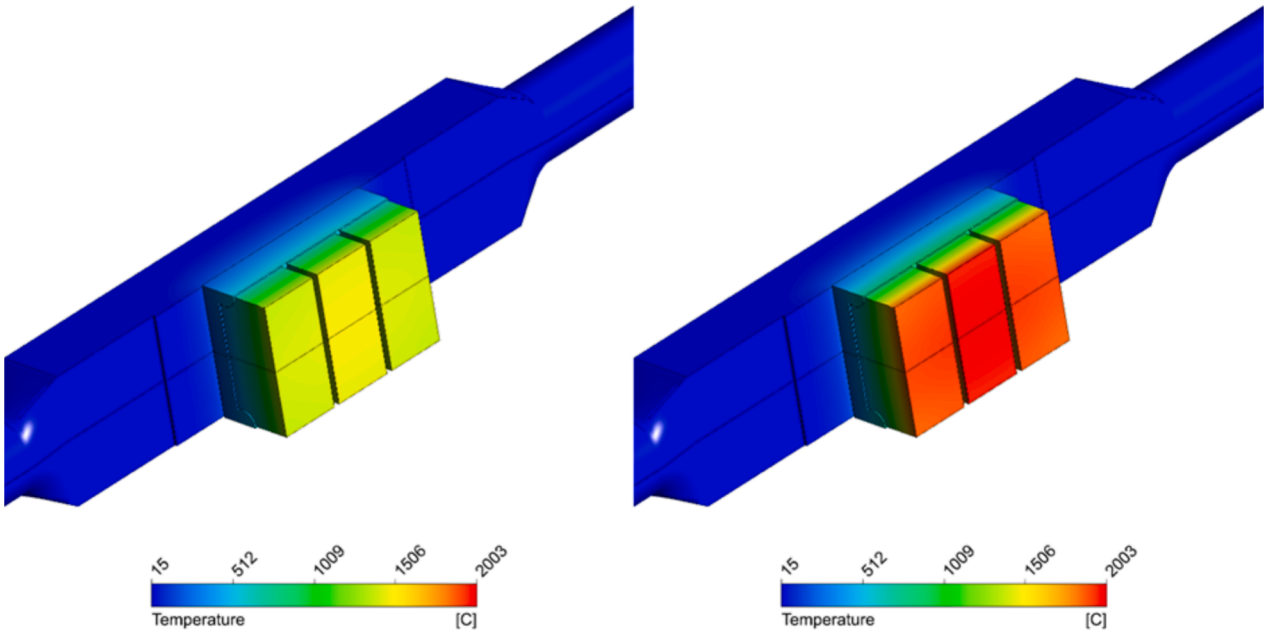

Fig. 31. Mock-up II steady-state temperature distribution during heating at 12 MW/m^2 (left picture) and 15 MW/m^2 (right picture).

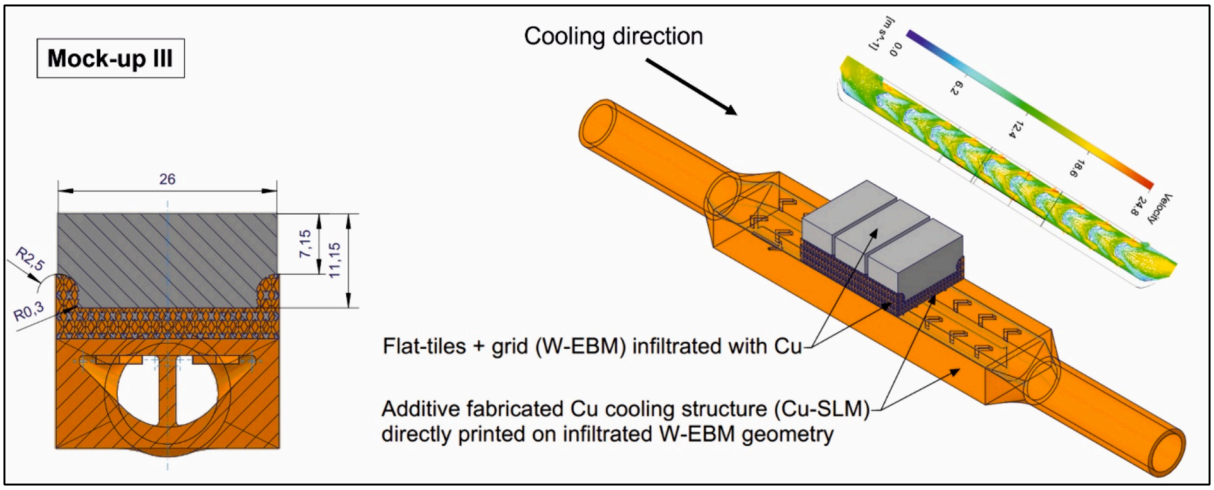

Fig. 32. Details of mock-up III.

mm). However, one should notice that, for the simulated case, the heat transfer is dominated by force convection, meaning that, the hyper-vapotron effect is not active. Fig. 36 display the simulation results of temperature distribution and coolant velocity near the wall of the cooling channel.

High heat flux testing at GLADIS

HHF testing of mock-up I

For the preliminary investigation screening pulses from 6 to 15 MW/m^2 are used, each with 20 s duration under room-temperature water-cooling conditions (T_{in} = 16 °C, v = 12 m/s, p_{in} = 15 bar). The conditions of the subsequent three test cycles are shown in Table 2.

Fig. 37 shows the IR images of the mock-up I of the 1st and the 100th pulse during the cycling at 20 MW/m^2. As Fig. 38 demonstrates, the screening and cycling in the cold-water loop was performed without any indication of cracks or damages.

HHF testing of mock-up II

The initial test for mock-up II was done using cold water-cooling conditions (T_{in} = 16 °C, v = 8 m/s, p_{in} = 14 bar) and started with a screening from 6 to 15 MW/m^2, with a pulse length of 20 s loading, followed by 100 cycles at 12 MW/m^2, 15 s on and 60 s off. The surface temperature of mock-up II at 12 MW/m^2 was 1980 °C. Fig. 39 shows the IR images of the mock-up II of the 1st and the 100th pulse of the HHF cycle at 12 MW/m^2. Screening and cycling at cold water-cooling conditions were performed without any formation of large cracks. Only at the left edge a small crack is visible (see Fig. 40). However, this was already visible during the 1st cycle.

The second test campaign applied to mock-up II was performed very similar to the first: cold water-cooling conditions (T_{in} = 16 °C, v = 8 m/s, pin = 14 bar), however a heat flux of 15 MW/m^2 up was applied (instead of 12) for 100 cycles with 15 s on and 75 s off periods. At 15 MW/m^2 the temperature on the surface of the mock-up II reached a value of 2650 °C in thermal equilibrium. Fig. 41 shows the IR images of the mock-up II from the 1st and the 100th pulse during the screening at 15 MW/m^2.

The visual inspection revealed no cracks or damages except the one

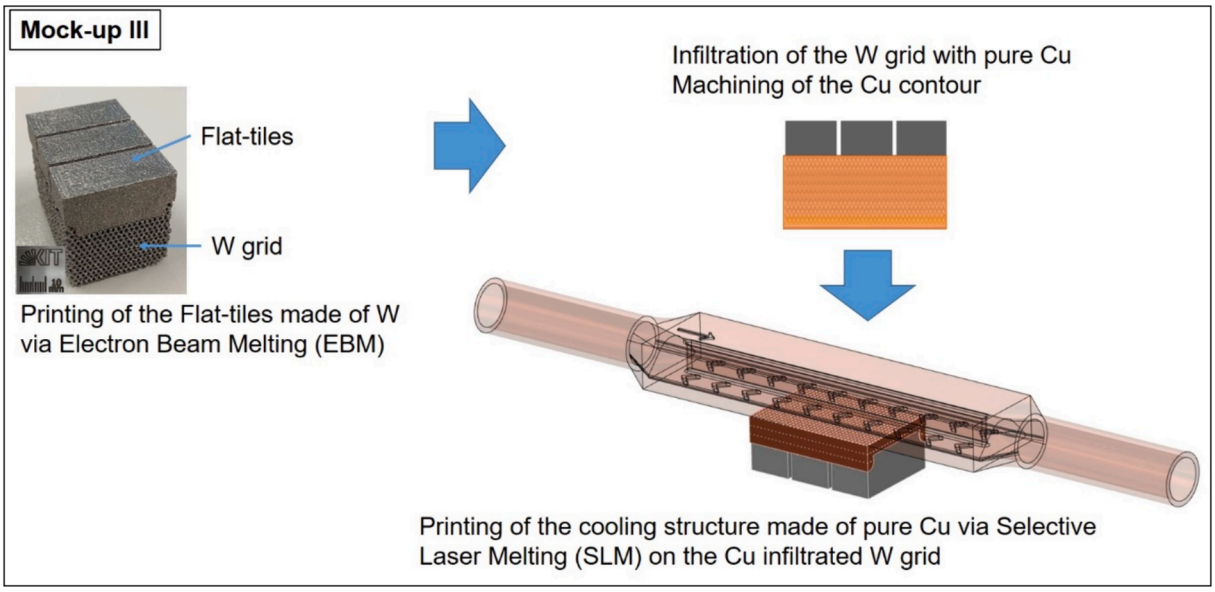

Fig. 33. Processing route of mock-up III.

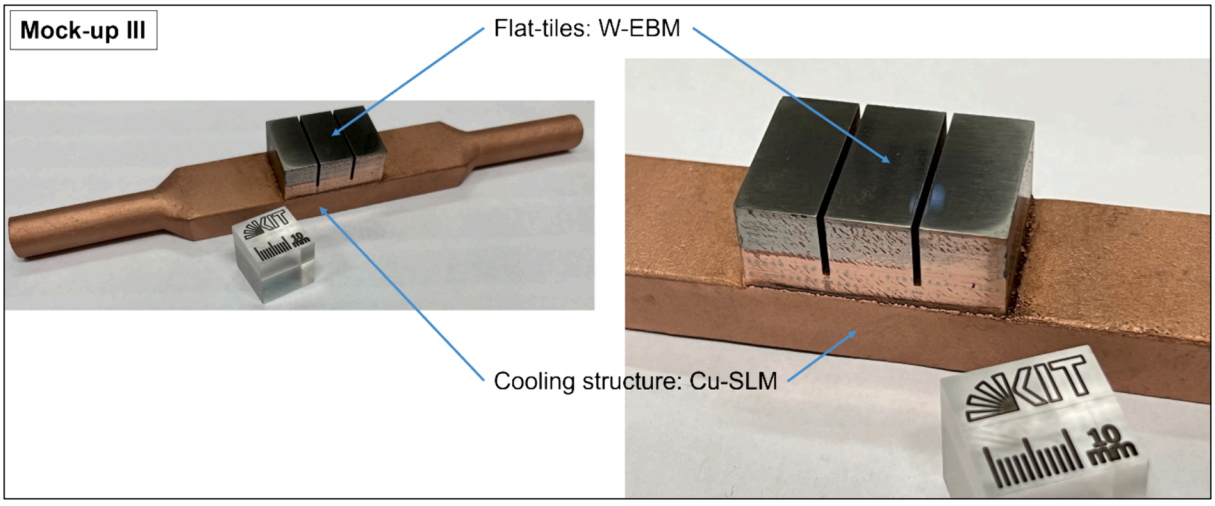

Fig. 34. Mock-up III. Combination of W-EBM and Cu-SLM w/o additional joining.

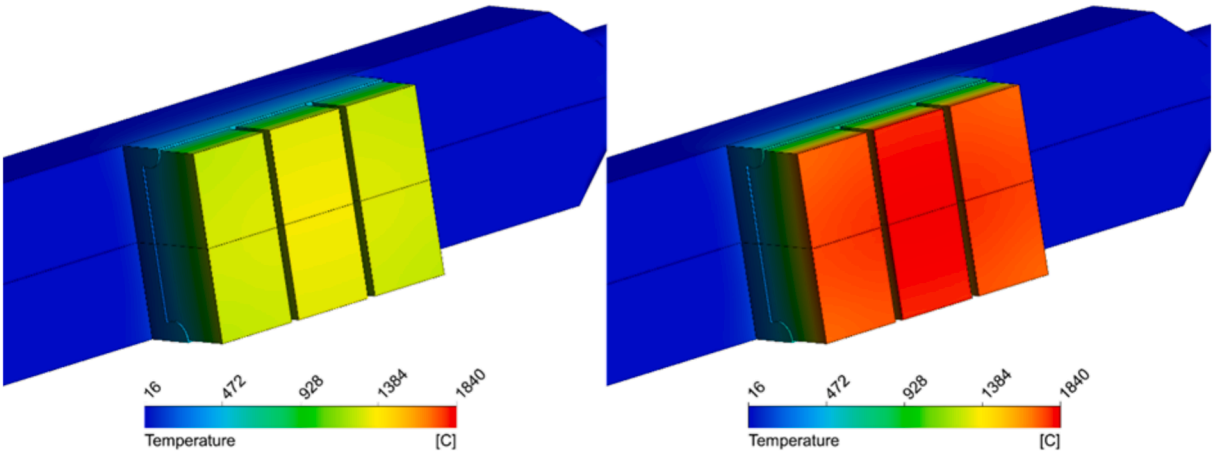

Fig. 35. ANSYS CFX simulation results of the Mock-up II temperature distribution if heated with a 12 MW/m^2 heat flux (left pictures) or with 15 MW/m^2 (right picture).

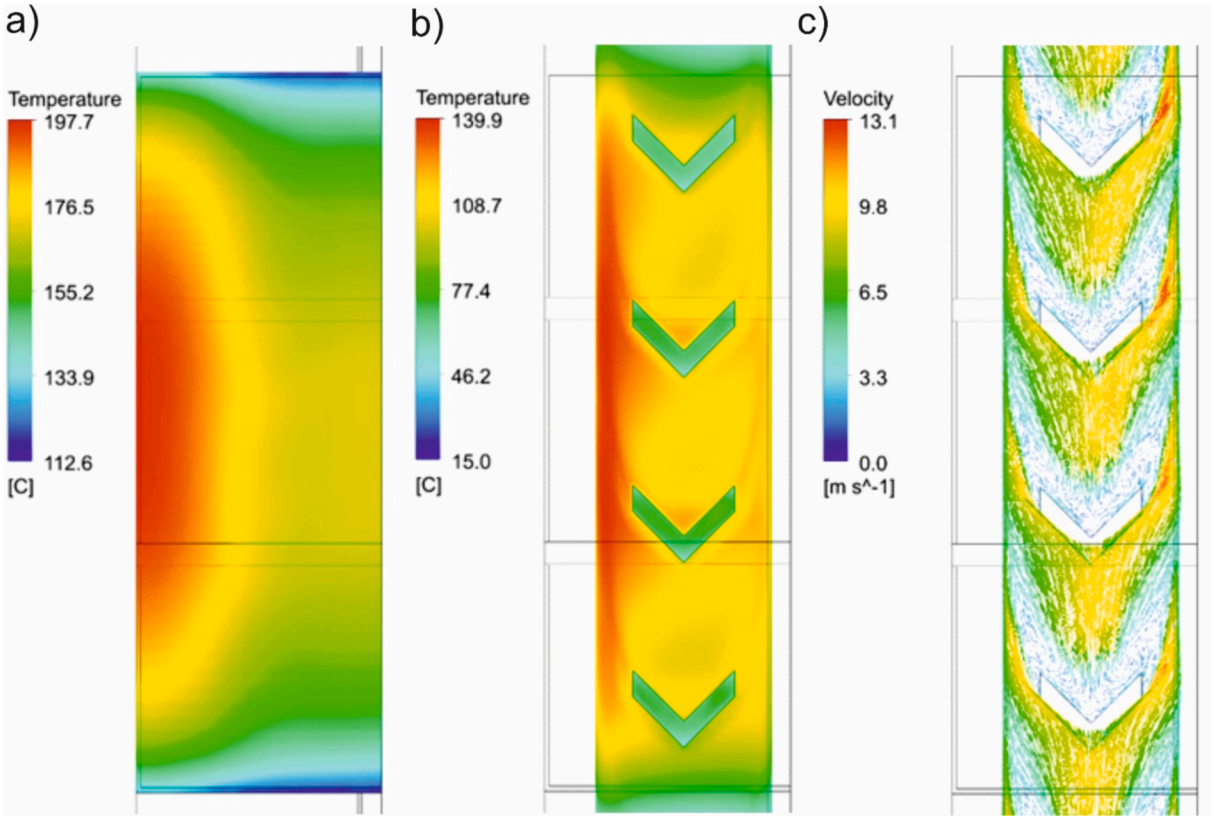

Fig. 36. Cooling channel temperature distribution and coolant velocity field near the wall. The pictures show only half of the mock-up surface on top of one of the two channels. (a) temperature of the copper body at the interface with the copper-tungsten composite; (b) wall temperature at the surface in contact with the coolant; (c) velocity field on a plane near the wall. Note that the water saturation temperature at 14 bar is around 195 °C, which is above the wall temperature (140 °C). Table 1 gives an overview.

Table 1
Overview of power, pressure, and temperature.

Mockup	Peak Heat flux /MW/m^2	p_{nom} /bar	T_{in} /°C	Flowrate /l/s	Surface temperature W1 /°C	Surface temperature W2 /°C	Surface temperature W3 /°C	Pressure loss /bar
MU-I	12	15.2	16	0.94	1076.7	1153.2	1081.7	1.15
	15	15.2	16	0.94	1457.6	1562.9	1463.3	1.15
	20	15.2	16	0.94	1998.8	2144.9	2004.9	1.15
MU-II	12	14	16	0.9	1401.2	1465.3	1404.8	2.30
	15	14	16	0.9	1891.4	1979.3	1895.8	2.32
MU-III	12	14	16	0.9	1281.6	1333.6	1284.4	0.67
	15	14	16	0.9	1744.3	1816.9	1748.0	0.66

Table 2
Test conditions for mock-up I.

No. of test	No. of cycles	Heat flux	Cycle length	Surface temperature
1	100	12 MW/m^2	15 s on, 60 s off	1600 °C
2	100	15 MW/m^2	15 s on, 75 s off	2100 °C
3	100	20 MW/m^2	15 s on, 105 s off	2520 °C

on the outer edge of one flat-tile (see Fig. 40).

HHF testing of mock-up III

For mock-up III, the initial test was done using cold water-cooling conditions (T_{in} = 16 °C, v = 8 m/s, p_{in} = 14 bar) and started with a screening from 6 to 15 MW/m^2, each pulse duration of 20 s, followed by 100 cycles at 12 MW/m^2, while the cycling scheme was 15 s on and 60 s off. The surface temperature of mock-up III was 1770 °C in equilibrium at 12 MW/m^2. Fig. 42 shows the IR images of mock-up III of the 3rd and the 100th pulse during the cycling HHF campaign at 12 MW/m^2.

Each of the three flat-tiles of mock-up III shows small surface cracks before testing (see Fig. 43, left). After the screening and cycling at cold water-cooling conditions, a new crack at the central block was detected (see Fig. 43, right). The reason for the cracks before testing could be explained by a failure during preparations for SLM printing the Cu cooling structure since after EBM printing no crack was detectable. The W-EBM structure was mechanically fixed in the SLM machine, which is believed to introduce high stresses in the tungsten flat-tiles during SLM printing of the cooling structure.

Post-mortem analyses after HHF tests in GLADIS

Fig. 44 shows the cross-section of mock-up I after HHF testing at GLADIS. No macroscopic failures of the tungsten flat-tiles were visible. However, a seam of some holes of the tungsten grid without copper

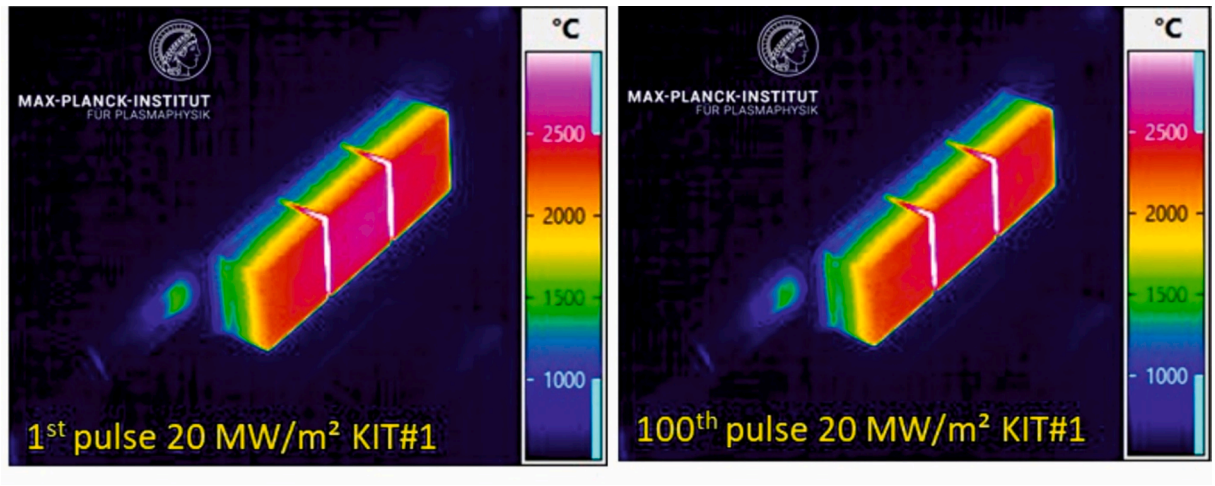

Fig. 37. Infrared (IR) image of mock-up I in the thermal equilibrium at 20 MW/m^2. The loaded surface of the three individual blocks (14.5 x 14.5 mm^2 each) shows a homogenous temperature distribution without any indication of local hot spots.

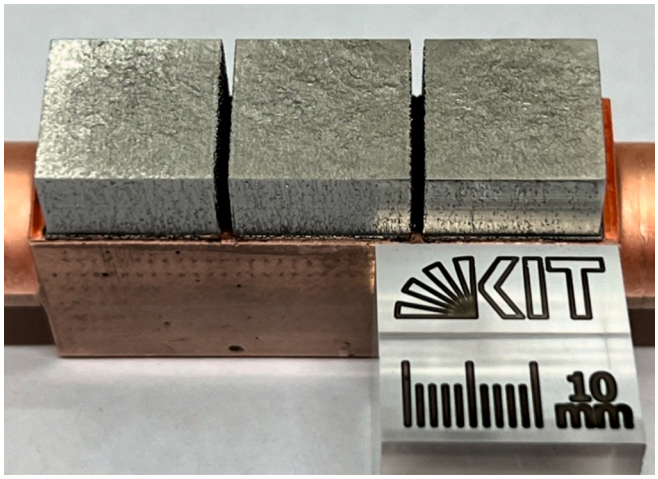

Fig. 38. Mock-up I. no cracks or damages after completion of GLADIS test program.

below the tungsten solid tiles became apparent (marked with red arrows). Here, the copper infiltration process or the tungsten grid needs to be optimized.

The visual inspection of mock-up II after the second test campaign (100 cycles at 12 MW/m^2 + 100 cycles at 15 MW/m^2) showed no more new cracks or damages except one thin crack on the outer edge of one flat-tile (see Fig. 40). Fig. 45 shows the copper-tungsten seam clearly, demonstrating that the copper infiltration and the following brazing process were successfully conducted.

Fig. 46 shows mock-up III after HHF testing at 12 MW/m^2. No damages and a faultless copper-tungsten seam after infiltration and brazing can be recognized.

Table 3 shows the different three mock-up designs, the reached results after the HHF testing and also the surface temperature during the test with the GLADIS facility. For mock-up I and II higher surface temperatures were measured. This is due to the cooling performance, the different height of the flat-tiles, and, in the case of mock-up I, the pores in the copper-tungsten seam.

Electron backscatter diffraction (EBSD) allows descriptive analyses of the grain size, orientation, distribution, and shape. Fig. 47 shows the microstructures of the initial state as EBM printed (columnar grain structure) and after HHF testing of the mock-ups. After HHF testing in GLADIS, for mock-up I and II the columnar microstructure has changed in the surface near region. Big grains near the surface have formed

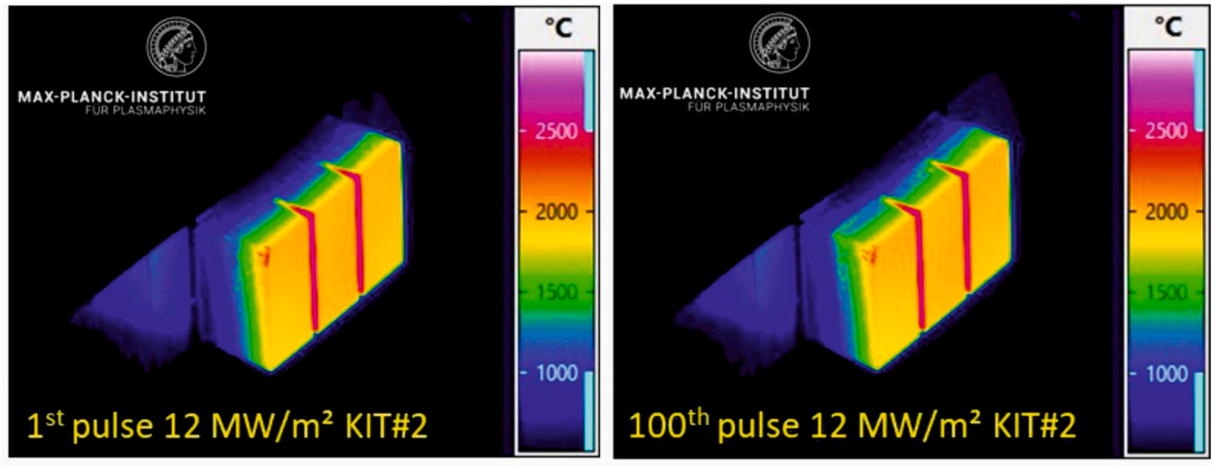

Fig. 39. IR image of the mock-up II during the screening at 12 MW/m^2. The loaded surface of the three individual blocks (26 x 12 mm^2 each) shows a homogenous temperature distribution except a local hot spot on the outer edge of the left block.

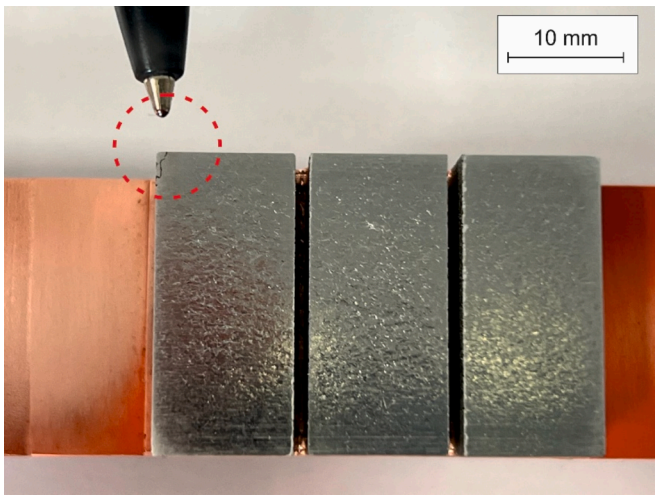

Fig. 40. Mock-up II. top side. the small crack on the left edge is highlighted after 100 cycles at 12 MW/m^2.

presumably due to recrystallization. The part below still consists of a columnar grain structure that originated in the EBM building process. A change of the microstructure after HHF testing of mock-up III could not be detected. It is concluded that the different response of the microstructure is related to the difference in surface temperature during the GLADIS testing as well as the varied numbers of test cycles of the three mock-up types. Furthermore, the various height of the tungsten flat-tiles is of importance (mock-up I: 8.3 mm, mock-up II: 11.5 mm, mock-up III: 11.15 mm).

Conclusions and outlook

The goal of this work was the fabrication of highly dense and crack-free tungsten parts via electron beam melting and the investigation of novel copper cooling structures for fusion applications. The main outcomes of this study can be summarized as follows:

EBM printed tungsten

Pure plasma-atomized tungsten powder was processed by electron beam melting in an Arcam A2X machine. The printed tungsten bulk samples exhibit a very high density of 99.8 % and a crack-free microstructure. Only some micropores were observed. The absence of microcracks can be explained by the low thermal stress due to the pre-

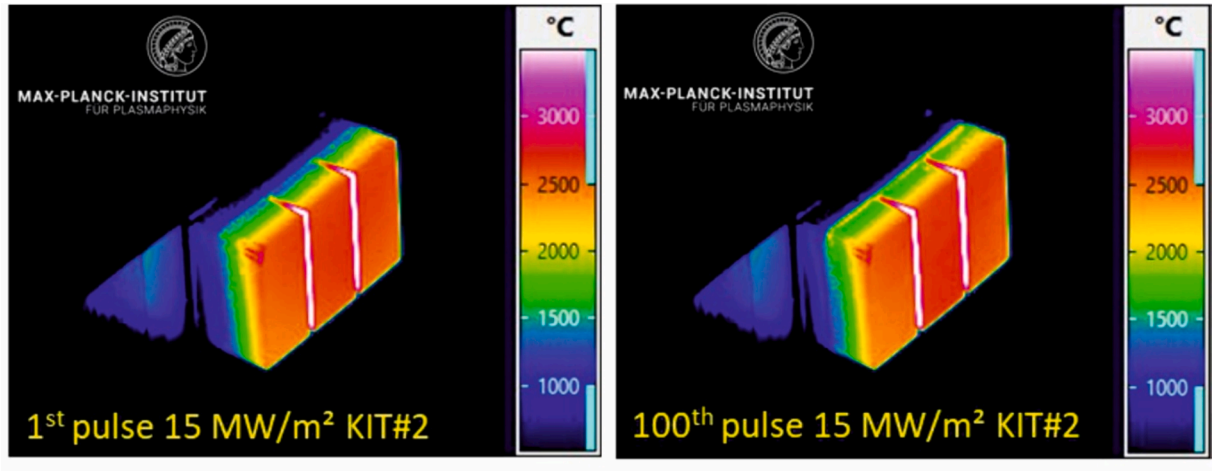

Fig. 41. IR image of the mock-up II during the screening at 15 MW/m^2.

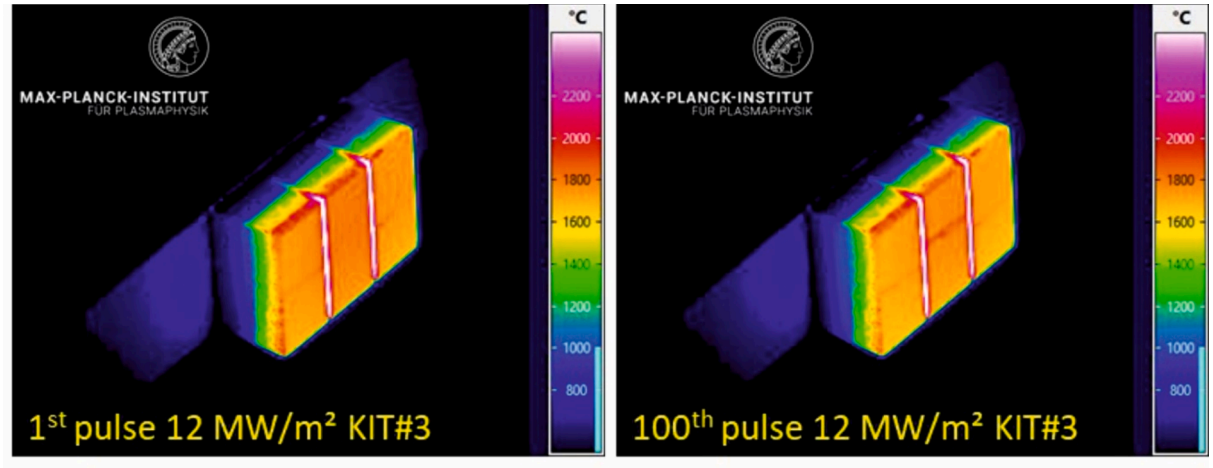

Fig. 42. IR image of mock-up III during cycling at 12 MW/m^2. The loaded surface of the three individual blocks (26 x 12 mm^2 each) shows at the beginning of cycling indications of small axial cracks in the left and right block. Surface inspection after the test confirmed the three visible cracks after 100 cycles.

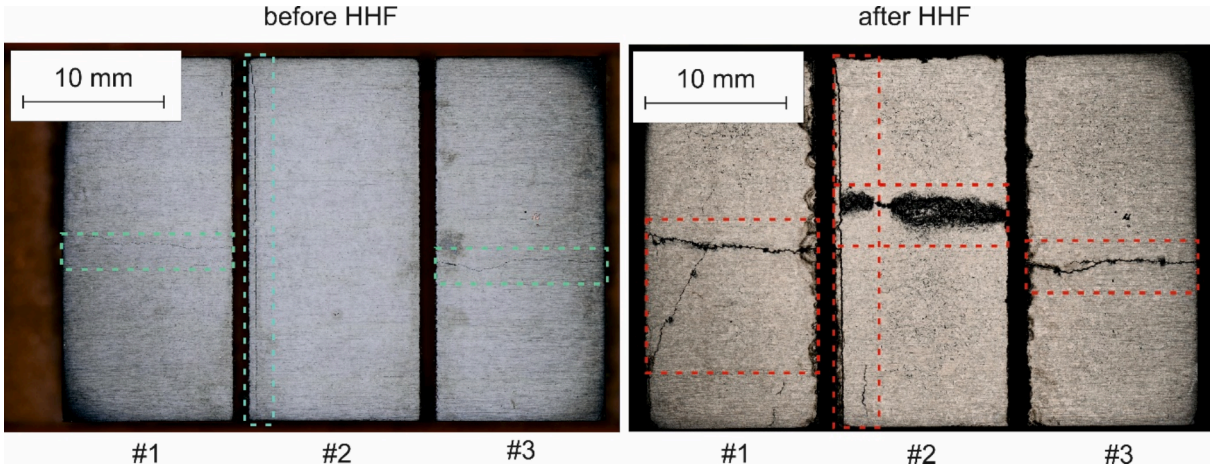

Fig. 43. Surface of mock-up III before HHF testing (left) and after HHF testing (right).

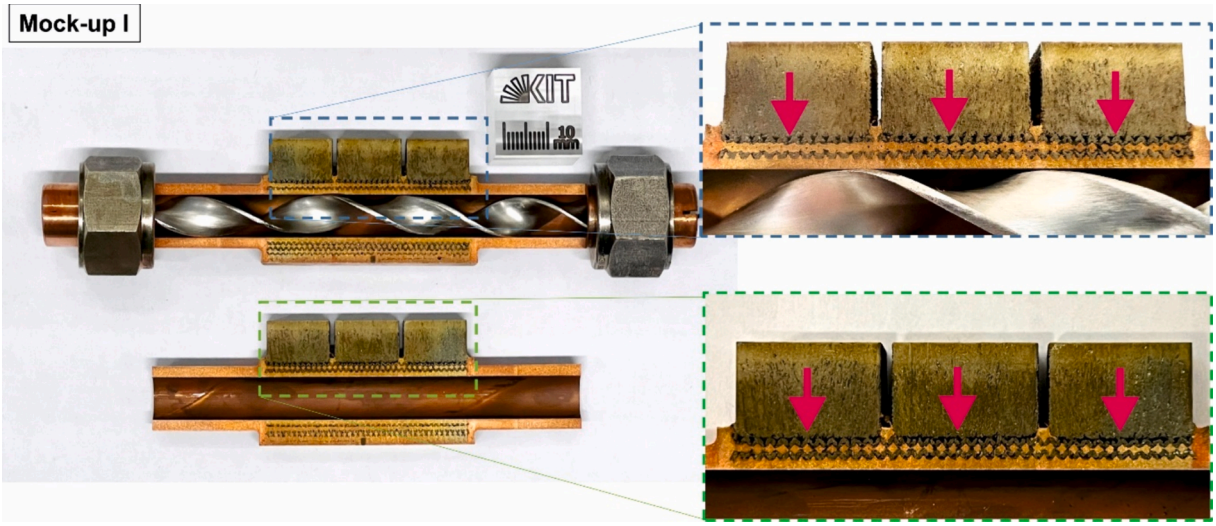

Fig. 44. Cross section of mock-up I after completed GLADIS HHF campaign (300 cycles).

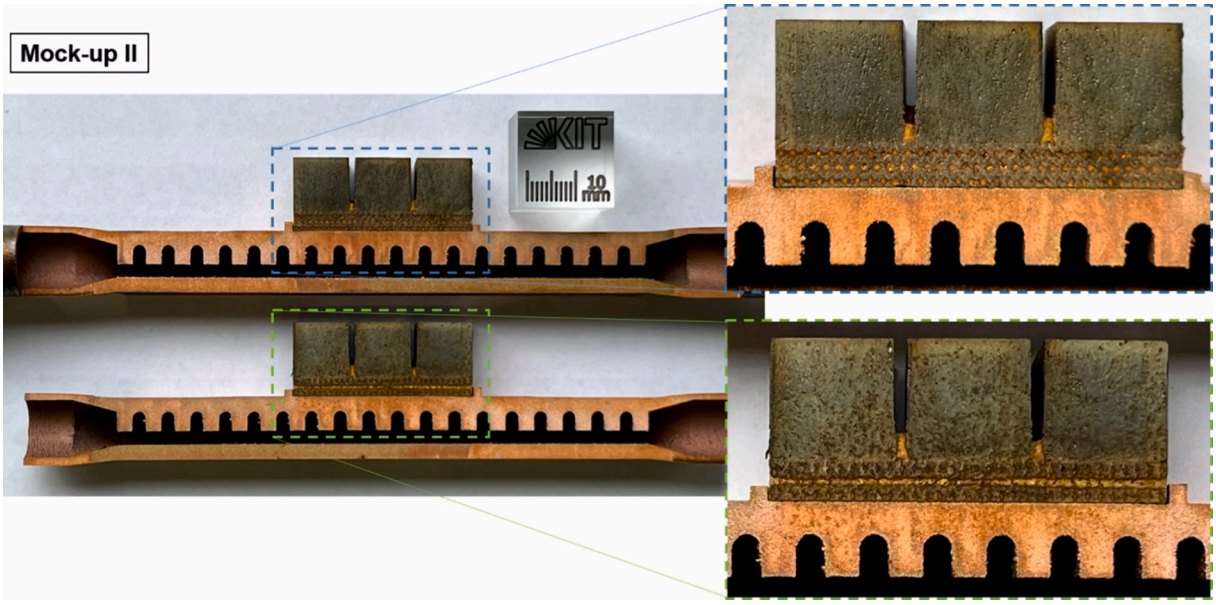

Fig. 45. Cross section of mock-up II (Hypervapotron) after completed GLADIS HHF campaign (200 cycles).

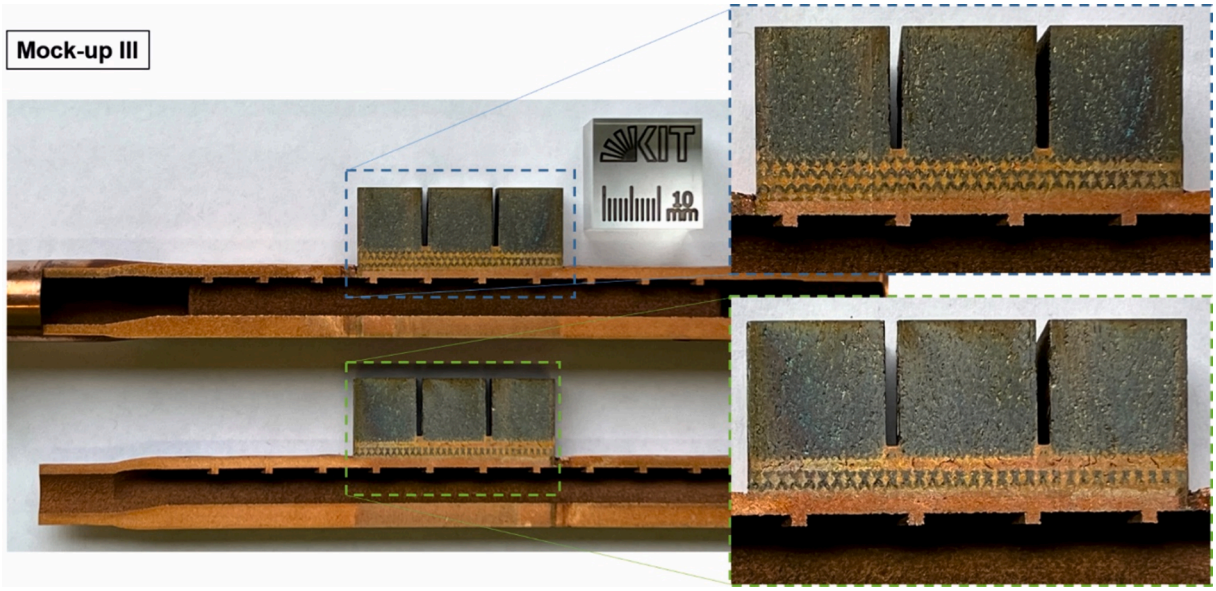

Fig. 46. Cross section of mock-up III after completed GLADIS HHF campaign (100 cycles).

Table 3
Parameters of the HHF Testing at GLADIS and measured surface temperature in thermal equilibrium.

Mock-up Design (unit: mm)	HHF Testing at GLADIS
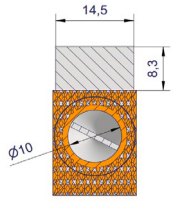	Mock-up I #1: 100 cycles at 12 MW/m^2; $T_{surface}$ = 1600 °C #2: 100 cycles at 15 MW/m^2; $T_{surface}$ = 2100 °C #3: 100 cycles at 20 MW/m^2; $T_{surface}$ = 2520 °C Cooling water conditions: v_{in} = 12 m/s, p_{in} = 15 bar
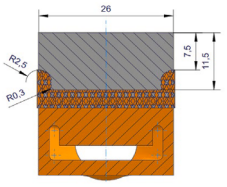	Mock-up II #1: 100 cycles at 12 MW/m^2; $T_{surface}$ = 1980 °C #2: 100 cycles at 15 MW/m^2; $T_{surface}$ = 2650 °C Cooling water conditions: v_{in} = 8 m/s, p_{in} = 14 bar
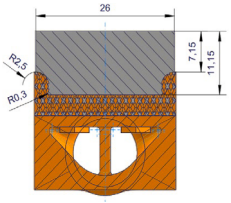	Mock-up III #1: 100 cycles at 12 MW/m^2; $T_{surface}$ = 1770 °C Cooling water conditions: v_{in} = 8 m/s; p_{in} = 14 bar

heating schemes during the EBM process and the reduction of oxide precipitates due to manufacturing in a vacuum environment. A long columnar grain structure along the building direction due to epitaxial growth seems to be typical for EBM-printed tungsten. This indicates a stable melt pool during the EBM process. The results of the tensile tests (test temperature range between 600 to 1000 °C) show a ductile behavior and total elongation of 80 % if tested along the building direction. It is concluded that the ductile-to-brittle-temperature (DBTT) for EBM tungsten is in the range between 700 to 900 °C. The measurement of the thermal conductivity corresponds to the literature for conventionally produced W. For the thermal shock testing at Judith 2 small tungsten cubes were loaded by an electron beam, simulating an ITER-like steady state (10 MW/m^2) and transient (10^5 pulses with 0.14 GW/m^2) heat loads simultaneously. No macroscopic failure was observed after this test.

Mock-up fabrication (W armour and pure Cu cooling structure)

For mock-up (MU) fabrication three different process routes are successful investigated: (MU I) pure copper melt infiltration of the EBM tungsten, (MU II) joining of the EBM tungsten tiles and the SLM copper cooling structure via brazing and (MU III) direct printing on the EBM tungsten tiles with a SLM printing process of a copper cooling structure. All process routes are stable: (MU I) w/o pores or microcracks, (MU II) the brazing joining zone was firm also after HHF testing w/o damage and (MU III) no joining zone was visible for the direct printing method and the join was steady.

Mock-up high heat flux testing at GLADIS

All three mock-ups successfully withstood the exposure to high heat fluxes at GLADIS. No macroscopic failures were visible, but due to the not optimized geometrical size (width and height) a very high surface temperature was reached which goes along with a big grain size near the surface after testing of mock-up I and mock-up II. However, the potential of the new cooling designs is evident: mock-up III showed no surface transformation and a lower surface temperature under the same cooling conditions as mock-up II with a heat flux of 12 MW/m^2. The minor surface temperature of the tungsten blocks in mock-up III is also influenced by the insignificant lower height of the tungsten blocks in comparison to mock-up II.

The results demonstrate successful the fabrication route of dense and crack free tungsten parts via electron beam melting and moreover the assembly to a component for testing. New investigations are planned with optimized geometrical dimensions (especially the flat-tile height) of the tungsten mock-ups fabricated via electron beam melting (EBM) and the use of CuCrZr cooling structures fabricated via laser powder bed fusion (L-PBF) instead of pure Cu. This next test campaign will be performed similar to DEMO hot water-cooling conditions (T_{in} = 130 °C, p_{in} = 40 bar) with a heat flux of 20 MW/m^2 up to 100 cycles for 10 s.

CRediT authorship contribution statement

Steffen Antusch: Writing – original draft, Methodology, Investigation, Formal analysis, Conceptualization. **Alexander Klein:** Writing –

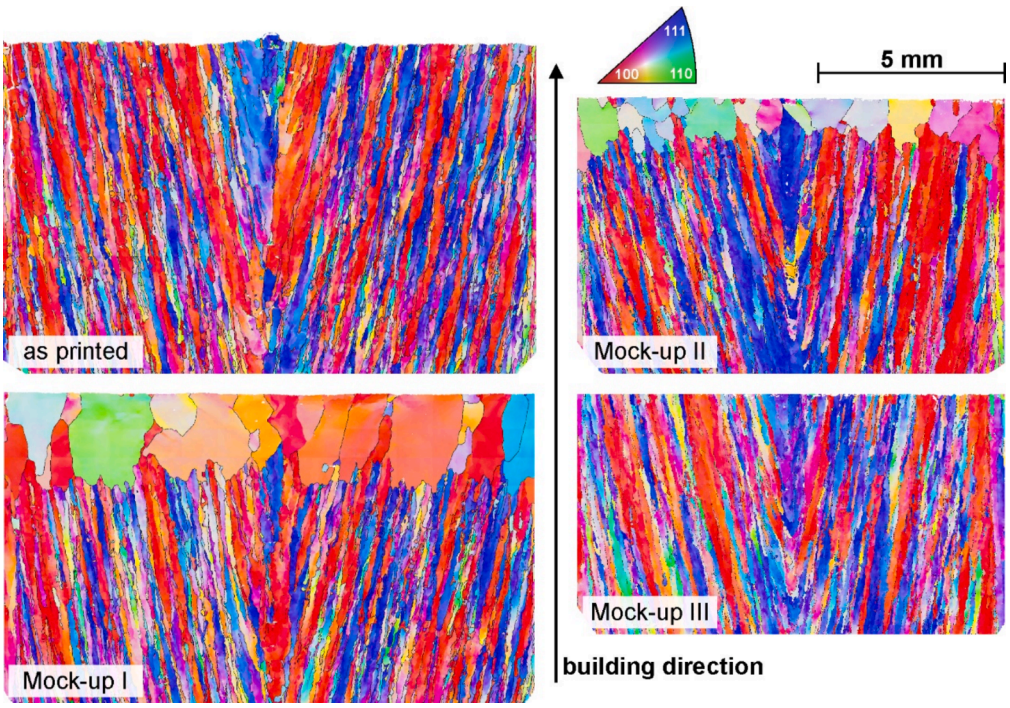

Fig. 47. Microstructure before and after HHF testing at GLADIS. The crystallographic directions refer to the building direction. The ruler is valid for all micrographs in this image.

review & editing, Methodology, Investigation, Conceptualization. **Siegfried Baumgärtner:** Investigation. **Carsten Bonnekoh:** Writing – review & editing, Investigation. **Bernd Böswirth:** Writing – review & editing, Investigation. **Daniel Dorow-Gerspach:** Writing – review & editing, Investigation. **Stefan Dietrich:** Writing – review & editing, Investigation. **Marco Ehrhardt:** Investigation. **Bradut-Eugen Ghidersa:** . **Henri Greuner:** Writing – review & editing, Investigation. **Markus Guttmann:** Investigation. **Thomas Hanemann:** Writing – review & editing, Resources. **Judith Jung:** Investigation. **Joachim Konrad:** Investigation. **Michael Rieth:** Writing – review & editing, Methodology, Conceptualization.

Declaration of competing interest

The authors declare that they have no known competing financial interests or personal relationships that could have appeared to influence the work reported in this paper.

Data availability

Data will be made available on request.

Acknowledgement

This work has been carried out within the framework of the EUROfusion Consortium, funded by the European Union via the Euratom Research and Training Programme (Grant Agreement No 101052200 — EUROfusion). Views and opinions expressed are however those of the author(s) only and do not necessarily reflect those of the European Union or the European Commission. Neither the European Union nor the European Commission can be held responsible for them. The authors are grateful to all their colleagues at the Karlsruhe Institute of Technology, Forschungszentrum Jülich, and Mrs. Katja Hunger at IPP Garching for the support and fruitful discussions. Mr. Daniel Bolich from KIT is especially acknowledged for his contribution.

References

[1] J.E. Emsley, The elements, 2nd ed., Oxford University Press, New York, 1991.
[2] E. Lassner, W.D. Schubert, Tungsten: Properties, Chemistry, Technology of the Element, Alloys, and Chemical Compounds, Springer, Berlin, 1999.
[3] M.G. Andrews, Tungsten, the Story of an Indispensable Metal, Tungsten Institute, Washington, 1955.
[4] M. Merola, D. Loesser, A. Martin, P. Chappuis, R. Mitteau, V. Komarov, R.A. Pitts, S. Gicquel, V. Barabash, L. Giancarli, J. Palmer, M. Nakahira, A. Loarte, D. Campbell, R. Eaton, A. Kukushkin, M. Sugihara, F. Zhang, C.S. Kim, R. Raffray, L. Ferrand, D. Yao, S. Sadakov, A. Furmanek, V. Rozov, T. Hirai, F. Escourbiac, T. Jokinen, B. Calcagno, S. Mori, ITER plasma-facing components, Fusion Eng. Des. 85 (2010) 2312–2322.
[5] J.H. You, E. Visca, T. Barrett, B. Böswirth, F. Crescenzi, F. Domptail, M. Fursdon, F. Gallay, B.-E. Ghidersa, H. Greuner, M. Li, A.v. Müller, J. Reiser, M. Richou, S. Roccella, Ch. Vorpahl: European divertor target concepts for DEMO: Design rationales and high heat flux performance, Nuclear Materials and Energy 16 (2018) 1–11.
[6] K.V. Shashank Sharma, M. Krishna, S.S. Joshi, M. Radhakrishnan, S. Palaniappan, S. Dussa, R. Banerjee, B. Narendra, Dahotre: Laser based additive manufacturing of tungsten: Multi-scale thermo-kinetic and thermo-mechanical computational model and experiments, Acta Mater. 259 (2023) 119244.
[7] F. Pixner, R. Buzolin, F. Warchomicka, A. Pilz, N. Enzinger, Wire-based electron beam additive manufacturing of tungsten, Int. J. Refract Metal Hard Mater. 108 (2022) 105917.
[8] C. Ledford, P. Fernandez-Zelaia, T. Graening, Q. Campbell, J.O. Rojas, A.M. Rossy, Y. Kato, M.M. Kirka, Microstructure and high temperature properties of tungsten processed via electron beam melting additive manufacturing, Int. J. Refract Metal Hard Mater. 113 (2023) 106148.
[9] S. Sharma, S.S. Joshi, M.V. Pantawane, M. Radhakrishnan, S. Mazumder, N. B. Dahotre, Multiphysics multi-scale computational framework for linking process–structure–property relationships in metal additive manufacturing: a critical review, Int. Mater. Rev. 68 (7) (2023) 943–1009.
[10] A. Talignani, R. Seede, A. Whitt, S. Zheng, J. Ye, I. Karaman, M.M. Kirka, Y. Katoh, Y. Morris Wang, A review on additive manufacturing of refractory tungsten and tungsten alloys, Addit. Manuf. 58 (2022) 103009.
[11] S.-H. Pan, G.-C. Yao, Y.-N. Cui, F.-S. Meng, C. Luo, T.-Q. Zheng, G. Singh, Additive manufacturing of tungsten, tungsten-based alloys, and tungsten matrix composites, Tungsten 5 (2023) 1–31.
[12] G. Rasiya, A. Shukla, K. Saran, Additive manufacturing-a review, Materials Today: Proceedings 47 (2021) 6896–6901.
[13] M. Tebianian, S. Aghaie, N.S.R. Jafari, S.R.E. Hosseini, A.B. Pereira, F.A. O. Fernandes, M. Farbakhti, C. Chen, Y. Huo, A review of the metal additive manufacturing processes, Materials 16 (2023) 7514.
[14] P. Gradl, D.C. Tinker, A. Park, O.R. Mireles, M. Garcia, R. Wilkerson, C. Mckinney, Robust metal additive manufacturing process selection and development for aerospace components, J. of Materi Eng and Perform 31 (2022) 6013–6044.

[15] D.-Z. Wang, K.-L. Li, C.-F. Yu, J. Ma, W. Liu, Z.-J. Shen, Cracking behavior in additively manufactured pure tungsten, Acta Metall. Sin. 32 (1) (2019) 127–135.
[16] K.L. Li, D.Z. Wang, L.L. Xing, Y.F. Wang, C.F. Yu, J.H. Chen, T. Zhang, J. Ma, W. Liu, Z.J. Shen, Crack suppression in additively manufactured tungsten by introducing secondary-phase nanoparticles into the matrix, Int. J. Refract. Met. Hard Mater. 79 (2019) 158–163.
[17] M. Guo, D. Gu, L. Xi, L. Du, H. Zhang, J. Zhang, Formation of scanning tracks during Selective Laser Melting (SLM) of pure tungsten powder: Morphology, geometric features and forming mechanisms, Int. J. Refract. Met. Hard Mater. 79 (2019) 37–46.
[18] A. Ivekovic, N. Omidvari, B. Vrancken, K. Lietaert, L. Thijs, K. Vanmeensel, J. Vleugels, J.-P. Kruth, Selective laser melting of tungsten and tungsten alloys, Int. J. Refract. Met. Hard Mater. 72 (2018) 27–32.
[19] A.V. Müller, G. Schlick, R. Neu, C. Anstätt, T. Klimkait, J. Lee, B. Pascher, M. Schmitt, C. Seidel, Additive manufacturing of pure tungsten by means of selective laser beam melting with substrate preheating temperatures up to 1000 °C, Nuclear Materials and Energy 19 (2019) 184–188.
[20] X. Ren, H. Liu, F. Lu, L. Huang, X. Yi, Effects of processing parameters on the densification, microstructure and mechanical properties of pure tungsten fabricated by optimized selective laser melting: From single and multiple scan tracks to bulk parts, Int. J. Refract. Met. Hard Mater. 96 (2021) 105490.
[21] G. Yang, P. Yang, K. Yang, N. Liu, L. Jia, J. Wang, H. Tang, Effect of processing parameters on the density, microstructure and strength of pure tungsten fabricated by selective electron beam melting, Int. J. Refract. Met. Hard Mater. 84 (2019) 105040.
[22] J. Wright, Additive Manufacturing of Tungsten via Selective Laser Melting and Electron Beam Melting, The University of Sheffield, Sheffield, UK, 2020. Ph.D. Thesis.
[23] D. Dorow-Gerspach, A. Kirchner, Th. Loewenhoff, G. Pintsuk, T. Weißgärber, M. Wirtz, Additive manufacturing of high density pure tungsten by electron beam melting, Nuclear Materials and Energy 28 (2021) 101046.
[24] https://go.additive.ge.com/rs/706-JIU-273/images/GE%20Additive_EBM_White%20paper_v3.pdf access date 04.03.2024.
[25] C. Körner, Additive manufacturing of metallic components by selective electron beam melting - a review, Int. Mater. Rev. 61 (2016) 361–377.
[26] ASTM International, Electrolytic Polishing of Metallographic Specimens, 9th ed. (E1558), ASTM International, West Conshohocken, PA, USA, 2014.
[27] R.W. Powell, C.Y. Ho, P.E. Liley, Thermal conductivity of selected materials, National Bureau of Standards, U.S. Dept. of Commerce, 1966.
[28] DIN EN ISO 14556:2017-05, Metallische Werkstoffe – Kerbschlagbiegeversuch nach Charpy (V-Kerb) - Instrumentiertes Prüfverfahren (ISO 14556:2015); Deutsche Fassung EN ISO 14556:2015 [in German]. https://www.beuth.de/de/norm/din- en- iso- 14556/272602371.
[29] T. Loewenhoff, et al., High pulse number thermal shock testing of tungsten alloys produced by powder injection molding, Nucl. Mater. Energy 20 (2019) 100680, https://doi.org/10.1016/j.nme.2019.100680.
[30] H. Greuner, B. Boeswirth, J. Boscary, P. McNeely, et al., High heat flux facility GLADIS: Operational characteristics and results of W7-X pre-series target tests, J. Nucl. Mater. 367–370 (2007) 1444–1448.
[31] E.A.I. Ellis, M.A. Sprayberry, C. Ledford, J.P. Hankwitz, M.M. Kirka, C.D. Rock, T. J. Horn, Y. Katoh, R.R. Dehoff, Processing of tungsten through electron beam melting, J. Nucl. Mater. 555 (2021) 153041.
[32] B. Vrancken, R.K. Ganeriwala, A.A. Martin, M.J. Matthews, Microcrack mitigation during laser scanning of tungsten via preheating and alloying strategies, Addit. Manuf. 46 (2021) 102158.
[33] Y.S. Touloukian, C. Y. Ho: Thermophysical Properties of Matter. Volume 4: Specific Heat, Metallic Elements and Alloys. IFI/Plenum, New York-Washington 1970. ISBN 0-306-67020-8.
[34] S.H. Lee, J.C. Kim, J.M. Park, C.K. Kim, S.W. Kim, Int. J. Thermophys. 24 (2003).
[35] J. Reiser, A. Hartmaier, Elucidating the dual role of grain boundaries as dislocation sources and obstacles and its impact on toughness and brittle-to-ductile transition, Sci Rep 10 (2020) 2739.
[36] A.V. Müller, D. Dorow-Gerspach, M. Balden, M. Binder, B. Buschmann, B. Curzadd, T. Loewenhoff, R. Neu, G. Schlick, J.H. You, Progress in additive manufacturing of pure tungsten for plasma-Facing component applications, J. Nucl. Mater. 566 (2022) 153760.
[37] Y. Wang, A.V. Dedov, An review for the heat transfer researches of Hypervapotron in the ITER first wall, Journal of Physics: Conference Series 1683 (2020) 022100, https://doi.org/10.1088/1742-6596/1683/2/022100.
[38] C.B. Baxi, H. Falter: A model for analytical performance prediction of hypervapotron. JETP920561, (1992) JET-P(92)56.
[39] G. Cattadori, G.P. Gaspari, G.P. Celata, M. Cumo, A. Mariani, G. Zummo, Hypervapotron technique in subcooled flow boiling CHF, Exp. Therm Fluid Sci. 7 (3) (1993) 230–240.
[40] A.R. Raffray, et al., Critical heat flux analysis and R&D for the design of the ITER divertor, Fusion Eng. Design 45 (1999) 377–407.